High-Power-Density Catalyst Induced Hydrino Transition (CIHT) Electrochemical Cell

R. Mills[1], J. Lotoski, J. Kong, G Chu, J. He, J. Trevey

BlackLight Power, Inc., 493 Old Trenton Road, Cranbury, NJ 08512, USA

Abstract: CIHT cells, each comprising a Mo, MoCu (50-50 at%), or MoNi (50-50 at%) hydrogen permeable membrane anode or tape cast CoCu, clad onto a hydrogen permeable Ni membrane, NiO cathode, a LiOH-LiBr eutectic mixture as the electrolyte, and MgO matrix in some cases, exploit hydrino formation as a half-cell reaction to serve as a new electrical energy source. The cells were operated under intermittent H_2O electrolysis to generate H at the anode and then discharged to form hydrinos wherein H_2O vapor as well as some O_2 was supplied from the atmosphere in open cells. Net electrical production over the electrolysis input and hydrogen supplied to the anode was measured to be multiples of the electrical input at about 10 mW/cm^2 anode area. The predicted molecular hydrino $H_2(1/4)$ was identified as a product of CIHT cells by MAS ^1H NMR, electron-beam excitation emission spectroscopy, Raman spectroscopy, X-ray photoelectron spectroscopy, and photoluminescence emission spectroscopy.

Key Words: new energy source, hydrogen catalysis, electrochemical cell, stable high power densities

[1] Corresponding author: 609-490-1090 (phone); 609-490-1066 (fax); rmills@blacklightpower.com

I. Introduction

Classical physical laws predict that atomic hydrogen may undergo a catalytic reaction with certain species, including itself, that can accept energy in integer multiples of the potential energy of atomic hydrogen, $m \cdot 27.2$ eV, wherein m is an integer. The predicted reaction involves a resonant, nonradiative energy transfer from otherwise stable atomic hydrogen to the catalyst capable of accepting the energy. The product is H(1/p), fractional Rydberg states of atomic hydrogen called "hydrino atoms," wherein n = 1/2, 1/3, 1/4,…, 1/p ($p \leq 137$ is an integer) replaces the well-known parameter n = integer in the Rydberg equation for hydrogen excited states. Each hydrino state also comprises an electron, a proton, and a photon, but the field contribution from the photon increases the binding rather than decreasing it, corresponding to energy desorption rather than absorption. A molecule that accepts $m \cdot 27.2\ eV$ from atomic H with a decrease in the magnitude of the potential energy of the molecule by the same energy may serve as a catalyst. The magnitude of the potential energy of H_2O is 81.6 eV [1]; so, the nascent H_2O molecule (not hydrogen bonded in solid, liquid, or gaseous state) may serve as a catalyst. Based on the 10% energy change in the heat of vaporization in going from ice at 0°C to water at 100°C, the average number of H bonds per water molecule in boiling water is 3.6 [1]; thus, H_2O must be formed chemically as isolated molecules with suitable activation energy in order to serve as a catalyst to form hydrinos. The catalysis reaction $(m = 3)$ regarding the potential energy of nascent H_2O is

$$81.6\ eV + H_2O + H\left[a_H\right] \rightarrow 2H^+_{fast} + O^- + e^- + H*\left[\frac{a_H}{4}\right] + 81.6\ eV \tag{1}$$

$$H*\left[\frac{a_H}{4}\right] \rightarrow H\left[\frac{a_H}{4}\right] + 122.4\ eV \tag{2}$$

$$2H^+_{fast} + O^- + e^- \rightarrow H_2O + 81.6\ eV \tag{3}$$

And, the overall reaction is

$$H\left[a_H\right] \rightarrow H\left[\frac{a_H}{4}\right] + 81.6\ eV + 122.4\ eV \tag{4}$$

The energy released to form hydrinos has been observed as continuum radiation in the 10-30 nm region and extraordinary fast H as reported previously [2]. In the present work, we show that the energy released by forming hydrinos according to Eqs. (1-4) gives rise to high-kinetic energy H. Using solid fuel Li + $LiNH_2$ + dissociator Ru-Al_2O_3 that can form H and HOH catalyst by decomposition of $Al(OH)_3$ and reaction of Li with H_2O and $LiNH_2$, ions arriving before m/e = 1 were observed by ToF-SIMS that confirmed the energy release of Eq. (4) is manifest as high kinetic energy H^-. We also report that XPS was performed on the solid fuel comprising Li + $LiNH_2$ + dissociator [3], and molecular hydrino $H_2(1/4)$ was confirmed as a product. The energy released to form hydrinos may ultimately be converted to thermal energy as

measured calorimetrically on solid fuels [2-4] and may be utilized in Rankine-style electrical power plants [5-6]. An alternative, more elegant system is directed to a hydrino fuel cell called a CIHT (Catalyst-Induced-Hydrino-Transition) cell that generates an electromotive force (EMF) from the catalytic reaction of hydrogen to lower energy (hydrino) states providing direct conversion of the energy released from the hydrino reaction into electricity. Each CIHT cell shown schematically in Figure 1 comprises a cathode, an anode, and an electrolyte that also serves as a source of reactants to form hydrinos. Due to oxidation-reduction half cell reactions, a hydrino-producing reaction mixture is constituted with the migration of electrons through an external circuit and ion mass transport through a separate internal path through the electrolyte to complete an electrical circuit. In one type of electrolytically regenerative CIHT cell reported previously [2], atomic hydrogen and oxygen are intermittently formed by electrolysis of H_2O in the cell, and the hydrogen catalyst and subsequent hydrinos are formed by a reaction of the reaction mixture during cell discharge with a net gain of electrical output.

Specifically, an exemplary prior tested CIHT cell [2] comprised a nickel mat anode, nickel oxide cathode, and the molten eutectic salt electrolyte LiOH-LiBr. The cell ran off of H_2O supplied as vapor to the cell entrained in an argon flow. The cell was operated under intermittent electrolysis and discharge. Hydrogen and oxygen were generated during the electrolysis phase at the negative and positive electrodes, respectively, and served as the sources of H and nascent H_2O catalyst. The catalyst forming reaction and the counter half-cell reaction that occurred during discharge are given by

Anode:

$$4OH^- + 4H_2 \rightarrow 4H_2O + 4e^- + 4H(1/p) \tag{6}$$

Cathode:

$$O_2 + 2H_2O + 4e^- \rightarrow 4OH^- \tag{7}$$

The overall reaction may be

$$4H_2 + O_2 \rightarrow 2H_2O + 4H(1/p) \tag{8}$$

wherein H_2O served as the catalyst. The electrolyte, operating temperature, and H_2O vapor pressure may be controlled such that the standard potential of the electron accepting reaction of Eq. (7) is at essentially 0 V relative to a standard hydrogen electrode to cause a better energy match of the product catalyst with H to facilitate the concerted reaction to hydrino according to Eq. (6).

The power of the hydrino reaction was manifest as an excess current at the operating voltage of the cell set by its conventional chemical composition. The hydrino-reaction-driven excess internal ion current was carried by oxygen containing ions involving oxidation-reduction

reactions of the electrolyte and added H_2O that occurred at the electrodes. Based on the Coulomb balance, the internal ion current was significantly manifested and propagated as the spontaneous electrolysis of water. Thus, once initiated, the hydrino reaction may produce electrical power with little to no input electricity as demonstrated experimentally. Exemplary ion-carrying, electrolyte-H_2O reactions that also result in H_2O electrolysis are

Anode:

$$2OH^- \rightarrow 2H + O_2^- + e^- \tag{9}$$

Cathode:

$$O_2^- + H_2O + e^- \rightarrow 1/2O_2 + 2OH^- \tag{10}$$

Anode:

$$2OH^- \rightarrow H + HOO^- + e^- \tag{11}$$

Cathode:

$$HOO^- + 1/2H_2O + e^- \rightarrow 2OH^- + 1/4O_2 \tag{12}$$

Anode:

$$3OH^- \rightarrow O_2 + H_2O + H + 3e^- \tag{13}$$

Cathode:

$$3/4O_2 + 3/2H_2O + 3e^- \rightarrow 3OH^- \tag{14}$$

wherein the hydrogen of Eqs. (9), (11), and (13) may react to form hydrinos:

$$2H \rightarrow 2H(1/4) \tag{15}$$

The overall reactions are

$$H_2O \rightarrow 1/2O_2 + 2H(1/4) \tag{16}$$

$$H_2O \rightarrow 1/2O_2 + H_2 \tag{17}$$

wherein the hydrogen of Eqs. (9), (11), and (13) may additionally react to form H_2O catalyst, and the oxygen of Eqs. (10), (12), and (13) may react and form OH^- according to Eqs. (6) and (7) respectively. Other oxygen species such as oxide, peroxide, superoxide, and HOO^- and corresponding oxidation-reduction reactions may be involved in the spontaneous electrolysis of H_2O to form at least one of H, catalyst, and hydrinos while carrying the excess current produced by the energy evolved from hydrino formation. Such closed CIHT cells with Ni anodes were validated by six independent expert scientists or teams to produce as high as 1000 times more electricity out than that required to electrolyze H_2O as the source of hydrogen to form hydrinos. These cells and other scale-up cells served as electrode and electrolyte samples for analytical analysis for the production of the theoretically predicted molecular hydrino product $H_2(1/4)$ that was identified. Albeit these first generation CIHT cells served as a proof of principle of the breakthrough new source of electricity, the power density was low, about 0.2 mW/cm^2 and correspondingly, the cell power was low, about 2-3 mW.

In the present paper, we report that the power density was increased by a factor of up to 500 times that of the prior CIHT cells. This was achieved by increasing the reaction rates at both the cathode and anode resulting in a higher hydrino catalytic rate. The oxygen reduction reaction in molten alkaline electrolytes is experimentally confirmed to be first order in O_2 partial pressure of an O_2-H_2O atmosphere favorable for forming the end-product oxygen ion OH^-. Albeit, O_2 is generated at the cathode during intermittent electrolysis, based on results of the effect of added O_2 pressure at increasing discharge currents, it was found that the cathodic oxygen reduction rate was limiting, and that atmospheric oxygen provides a much higher partial pressure than internal electrolysis at any cell current tested (up to 150 mA). Thus, the cells were run open to the atmosphere that provided H_2O vapor as well as O_2. The goal was to produce electrical gain over that of intermittent electrolysis while maintaining a thermodynamic anode voltage that would be sufficiently negative to avoid corrosion. Using open cells, the Ni foil was found to support much less current than the Ni celmet anode that supported slightly greater than 0.2 mW/cm^2, but a high cell voltage could not be maintained, and some anode weight loss was experienced. To further protect the anode, a hydrogen permeable membrane was substituted. It was found that the H permeable anode could support much higher power density without weight loss, about a time-averaged anode power density of 2-3 mW/cm^2. But, the maximum theoretical electrical power of the hydrogen flow by permeation forming H_2O was comparable; so, the excess electricity was low. The combination of stability and gain was achieved by two approaches. In one case, Mo and Mo alloys (MoCu (50-50 at%) or MoNi (50-50 at%) were used as the anode material wherein the power densities even for foils was up to 500 times higher than that of Ni celmet. Using Mo-based foil anodes of available thickness, electrical power output was typically about two times the electrical input and in some cases exceed the input by a factor of greater than 5 at >10 mW/cm^2 anode. In this case, the hydrino contribution to the power was sufficiently high at a corrosion-protective thermodynamic anode voltage that it overwhelmed the contribution due to H permeation that further protected the anode. The power density was increased by a factor of over 10 by running a correspondingly high current without sufficient H corrosion suppression due to a limited H permeation rate, but the results indicate that thinner, more permeable foils should provide long-term stability with high electrical gain.

Additionally, the power is expected to increase substantially with the use of high surface area materials. The Ni anode was shown to be stable at higher power densities of 5 mW/cm^2 while maintaining the same voltage as the Ni celmet by using high surface area tape cast material. Ni-Co (95-5 at%) powder was tape cast onto a hydrogen permeable Ni membrane, or a sparging tube was supplied to the middle of tape case encasing a porous support. Hydrogen was supplied such that the weight loss was avoided with the production of a slight excess of electricity over the sum of the contributions due to electrolysis and permeation or sparging.

Even better gain performance was obtained with anodes comprising tape cast CoCu (82-18 wt%) clad onto a Ni permeable membrane. These anodes were found to be very stable in LiOH-LiBr electrolyte and developed about 7.3 mW/cm^2 at about two times the energy gain with only a 10% input energy contribution from hydrogen permeation. A similar factor of 25 times increase in power density can be expected for Mo based anodes of high surface area, but at much higher net power relative to the total of the contributions from electrolysis and permeation. The predicted molecular hydrino $H_2(1/4)$ was identified as a product of the CoCu tape cast as well as Mo-based and CIHT cells by MAS ^1H NMR, electron-beam excitation emission spectroscopy, Raman spectroscopy, and photoluminescence emission spectroscopy.

II. Experimental

CIHT cell electrical energy balance

An exemplary CIHT cell comprised (i) a 6.5 cm ID X 14 cm IH alumina crucible containing the cell components, (ii) a MoCu (50-50 at%, AMETEK), 3.8 cm OD, 11 cm^2, submersed in electrolyte; alternatively, Mo or MoNi alloy (50-50 at%) foil anode, 1 X 1 cm, $1cm^2$, 1.1 g and 1.2 g, respectively, (iii) a NiO cylindrical cathode, 3.8cm OD x 1cm ID x 5cm tall, pre-oxidized porous Ni CNi6 (Sumitomo Electric oxidized in air at 800°C for 4 h) placed on top of electrolyte, and (iv) a molten eutectic salt electrolyte comprising LiOH (15 g)-LiBr (75 g) and optionally a MgO matrix (30 g). The electrode spacing was 0.2-0.3 cm maintained by an alumina separator ring. The alumina crucible containing the cell components was placed in a resistive heater that maintained the temperature of the electrolyte at 430 ± 2 °C. The cell was operated open to atmosphere. A CIHT permeation cell comprised the standard design with a hydrogen permeable anode substituted for the foil anode. The cell anode was a H_2 permeable Mo, MoCu (50-50 at%, AMETEK), or MoNi (50-50 at%) diaphragm made of two pieces of 1.5" OD and 0.020" thickness foils welded together and joined to a 1/4" (OD) Ni H_2 supply tube. A CoCu (82-18 wt%) tape cast anode 1.5" OD that was clad onto a 7/8" OD H_2 permeable 0.010" thick Ni membrane was of the same construction as the Mo and MoCu membranes by 2 ton compression. The hydrogen was supplied from a two liter tank having a H_2 pressure in the range of 950 ± 30 Torr monitored using a Baratron gauge.

Co-Cu (82-18 wt%) anodes were made by a tape casting and sintering process. The tape casting slurry was prepared by ball milling Co and Cu powders in water with polyvinyl alcohol (PVA) as a binder and glycerol as a plasticizer. Two steps were involved in the ball milling. First, 45 g Co powder (Aldrich, particle size: 2 um) was mixed with 10.00 g Cu powder (Aldrich, 3 um). 5.0 g PVA (Aldrich) dissolved in 38 g deionized H_2O was added into the metal powder

mixture and mixed thoroughly. The slurry was ball milled for 2h. Next, 9.0 g glycerol was added to the above suspension, and the mixture was further ball milled for another 2 h. The slurry was then cast on Ni celmet plate (CNi 4 Ni foam, ~12"x10") using a home-made doctor blade (tape cast tool) assembly. The cast was dried at ambient temperature for 24 h. The plate was then cut into smaller pieces (e.g., 1.5" diameter disc) and placed inside a tubular furnace for sintering at 820 °C under the flow of 20% H_2-80% Ar mixture (10 ml/min). The furnace temperature was ramped from room temperature to 820 °C in 4 h, and held at 820 °C for another 2 h. Then, the furnace was cooled down to room temperature in 1 h. The sintered Co-Cu discs were then fabricated into anodes.

The pre-lithiated Ni cathode was made by a tape casting and oxidation sintering process. First, 52.70g Ni-255 powder (Novamet, type 255) was mixed with 3.80g Li_2CO_3 powder (Aldrich, 99 wt%) and 8.0 g PVA (Aldrich). 38g of DI H_2O was added to the mixture with stirring. The slurry was ball milled for 2h. Next, 9.5 g glycerol was added to the suspension, and the mixture was further ball milled for another 2 h. The slurry was then coated onto both sides of a Ni celmet plate (CNi 4 Ni foam, ~12"x10") using a paintbrush. The cast was dried at ambient temperature for 24 h. The plate was then cut into 3.0" x 9" strip, which was then rolled into a ~3/8" ID (~1.0 cm), 2.25" OD (5.7 cm) and 3" (7.5 cm) height cylindrical roll and placed inside a kiln furnace for sintering at 800 °C in air. The furnace temperature was ramped from room temperature to 800 °C in 3 h, and held at the same temperature for another 2 h. Then, the furnace was gradually cooled to room temperature. The sintered pre-lithiated NiO cylindrical rolls were used to fabricate the cathode.

Nickel leads from the anode and stainless steel leads from the cathode were attached to the leads of an Arbin BT2000 fuel cell and battery testing system calibrated within 6 months of usage at Arbin Instruments (College Station TX). The cell was run under intermittent electrolysis conditions. Typically, the programmed waveform comprised the steps of (i) charge at 50 mA constant current for 1s duration and (ii) discharge at 50 mA constant current for 2s duration. Alternatively, the waveform was (i) charge at 50 or 100 mA constant current until the cell voltage reached 0.9 V and (ii) discharge at 50 or 100 mA constant current until the first of either the cell voltage reached 0.85 V or 1s duration. The Arbin BT2000 voltage, current, power waveforms, and energy were confirmed with a digital oscilloscope. Compositional and elemental analyses of the electrolyte were performed by inductively coupled plasma mass spectroscopy (ICPMS), X-ray fluorescence (XRF), and X-ray diffraction (XRD). The anode structure was confirmed intact using scanning electron microscopy (SEM) with elemental analysis by energy-dispersive X-ray spectroscopy (SEM-EDX).

Digital oscilloscope oonfirmation of the CIHT oell electrical energy balance

The Arbin measurements were confirmed with a data acquisition system (DAS) comprising a PC with Labview 6033E data acquisition card and Labview VI, SCB100 breakout box, and two differential input channels: one being a voltage channel biased to ground across a 5 MΩ resistor, and the other being a voltage channel measuring current by an IR drop across a 1 Ω 1% precision resistor also biased to ground across a 5 MΩ resistor. The DAS was tested against a NIST traceable calibrated Fluke 45 and the voltage and current measurement were confirmed to be accurate to within ~1 mV, < 1 mA. The DAS was also tested against a dual square waveform generated by an Agilent 33220A 20 MHz Arbitrary Waveform Generator and compared to a Tektronix TDS 3054B 500 MHz 5 GS/s Oscilloscope. The major test waveform comprised a 2 Hz cycle, 300 ms on pulse, 0.2 V p-p, and the minor test waveform comprised a 166 Hz cycle, 600 μs on pulse, 40 mV p-p. Sample data was obtained at 10 KS/s on both the DAS and oscilloscope and both the major and minor waveforms were clearly resolved, and V*t areas matched to within 0.6%.

Analytical samples for the spectroscopic identification of molecular hydrino

CIHT cells having a molten LiOH-LiBr and optionally MgO electrolyte and a single electrode set or a stack of CIHT cells having bipolar-plate electrodes served as sources of the theoretically predicted molecular hydrino product $H_2(1/4)$. Magic angle spinning ^1H nuclear magnetic resonance spectroscopy (MAS ^1H NMR), electron-beam excitation emission spectroscopy, Raman spectroscopy, and photoluminescence emission spectroscopy were performed on reaction products. The molecular hydrino samples comprised CIHT electrolyte, CIHT electrodes, and inorganic compound getters such as KCl-KOH mixture placed in the sealed container of closed CIHT cells wherein hydrinos generated during operation were trapped in the matrix of the compound that thereby served as a molecular hydrino getter. Starting materials not exposed to a hydrino source served as controls.

Quantitative X-ray diffraction (XRD)

XRD was performed on the starting materials and the reaction products using hermetically sealed sample holders (Bruker Model #A100B37) loaded in a glove box under argon, wax sealed, and analyzed with a Siemens D5000 diffractometer using Cu radiation at 40kV/40mA over the range 10° – 80° with a step size of 0.02° and a counting time of 143 seconds per step. Once the

patterns had been obtained, the phases were identified with the aid of the ICDD database and quantified by a Rietveld refinement.

Scanning Electron Microscopy (SEM)/Energy-Dispersive X-ray Spectroscopy (EDX)

Surface microstructures of various electrodes were studied by scanning electron microscopy (ESEM, Quanta 200 FEG). The elemental composition was analyzed by EDX using the same instrument.

MAS ^1H NMR

^1H MAS NMR was performed on solid samples using a 270 MHz instrument with a spin speed of 4.5 kHz. Chemical shifts were referenced to external TMS.

UV Spectroscopy of Electron-Beam Excited Interstitial $H_2(1/4)$

Vibration-rotational emission of $H_2(1/4)$ trapped in the lattice of a CIHT cell MoCu anode was investigated via electron bombardment of the crystals. Windowless UV spectroscopy of the emission from the electron-beam excitation was recorded using a McPherson 0.2 meter monochromator (Model 302, Seya-Namioka type) equipped with a 1200 lines/mm holographic grating with a Al-MgF_2 coating and a photomultiplier tube (PMT) detector. The wavelength resolution was 1.5 nm with an entrance and exit slit width of 500 μm. The increment was 1 nm and the dwell time was 5 s.

Raman Spectroscopy

Raman spectroscopy was performed on solid samples using a Horiba Jobin Yvon LabRAM Aramis Raman spectrometer with a 325 nm that HeCd laser was operated in microscope mode with a magnification of 40X. Additionally, spectra were obtained on anodes before and after sonication in deionzed H_2O and well as bulk samples in glass vials using a Thermo Scientific DXR SmartRaman spectrometer having a 780 nm diode laser. The resolution, depending on the instrument focal length, wavelength range, and grating, was typically 1 - 5 cm^{-1}.

FTIR Spectroscopy

FTIR analysis was performed on solid-sample pellets using the transmittance mode of Nicolet 730 and Nicolet 6700 FTIR spectrometers each with a DTGS detector. The samples were handled under an inert atmosphere. The resolution was 1 cm^{-1}.

ToF-SIMS Spectroscopy

Solid fuel Li + $LiNH_2$ + dissociator Ru-Al_2O_3 was characterized using a PHI TRIFT V nanoTOF ToF-SIMS instrument. The primary ion gun utilized a Ga source. In order to remove surface contaminants and expose a fresh surface, the samples were sputter-cleaned for 30 seconds prior to data collection. The aperture setting was 100 μm. Data were collected up to 2000 AMU in positive and negative ion modes using three raster sizes/ion doses for each sample: 100 μm X 100 μm, $5.5\ X\ 10^{11} ions/cm^2$; 50 μm X 50 μm, $2.2\ X\ 10^{12} ions/cm^2$; 25 μm X 25 μm, $8.8\ X\ 10^{12} ions/cm^2$. During acquisition, the ion gun was operated using a bunched (pulse width 4 ns bunched to 1 ns) 30 kV beam. The stage voltage was 3 kV. Charge neutralization was active, and the post accelerating voltage was 4 kV.

XPS Spectra

A series of XPS analyses were made on electrode and crystalline samples using a Scienta 300 XPS Spectrometer or a Kratos Analytical Axis Ultra. The fixed analyzer transmission mode and the sweep acquisition mode were used. The step energy in the survey scan was $0.5\ eV$, and the step energy in the high-resolution scan was $0.15\ eV$. In the survey scan, the time per step was 0.4 seconds, and the number of sweeps was 4. $C\ 1s$ at $284.5\ eV$ was used as the internal standard.

III. Results and Discussion

A. CIHT Cell Electrical Energy Balance

The cell construction details, operating temperature, intermittent electrolysis parameters, and cell charge energy, discharge energy, and electrical gain at timed intervals for a representative CIHT cell [MoCu (H permeation)/LiOH-LiBr-MgO/NiO] are given in Table 1. The exemplary charge and discharge waveform recorded by the digital oscilloscope (Figure 2) for a repeated exemplary cell shows that the input charging time to achieve the set point of 1.02 V was 1.058 s; where

after, the cell discharged for 2.058 s to reach the set voltage of 0.94V. The digital oscilloscope measured energy balance matched that of the Arbin system within a few percent. The excess current over the corresponding input Coulombs shown in Figure 2 was carried by the H_2O and electrolyte ion reactions given in Sec. I. The resulting excess discharge current at the nominal charge voltage resulted in a high electrical energy gain. The electrical power was essentially constant over two and a half days of operation wherein the energy generated during discharge was 1.879 Wh compared to 1.078 Wh of input H_2O electrolysis energy at an overall gain of about 1.76 times. A plot of the voltage and accumulated input and output energies over the duration of the run are given in Figure 3. The hydrogen consumption was about 2.62 X 10^{-8} moles/s yielding a maximum possible energy contribution from H_2 of 0.355 Whr, resulting in a net contribution of 0.446 Whr from the hydrino reaction. In permeation cells run longer than 72 hours, the hydrogen consumption gradually dropped to zero over the three days, and thereafter no hydrogen was consumed wherein the electrolysis hydrogen maintained a steady state H_2 pressure.

Similar results were obtained for cells with Mo or MoNi anodes ([Mo or MoNi alloy (H permeation)/LiOH-LiBr-MgO/NiO]). Mo and Mo alloy cells were found capable of supporting power densities as high as 100 mW/cm^2 over a 60-hour duration, operating at above 0.8 V. However, the H flow rate was insufficient to prevent some weight loss. Based on the 2.62 X 10^{-8} moles/s cm^2 hydrogen flow that prevented weight loss of Mo or Mo alloy H permeable membranes at the same 100 mA/cm^2, it is projected that the use of a thinner membrane than the 0.1 cm thick membrane used will provide sufficient H to avoid weight loss while contributing a small fraction to the theoretical input power. The Mo and Mo alloy cells all produced hydrino products. For representative cells, the data of the identification of the predicted molecular hydrino product $H_2(1/4)$ with the corresponding energy balance parameters are given in Sec. IIIB.

Alternative sources of the excess electricity comprise the metal-air battery reaction, however, the anode was removed, sonicated, dried, leak checked with helium to confirm that no electrolyte and its associated weight were added to the electrode, and weighed. No weight loss was observed within experimental error. As a measure of the definitiveness of this result, consider Mo of the anode oxidized at the free energy of 541 kJ/mole Mo (Table 2) for the reaction Mo + $3/2O_2$ to MoO_3. Then, in order for the net energy to be accounted by conversion of Mo metal to oxide at 100% electrical efficiency, 0.3 g would have to be lost selectively. The theoretical voltages E_0 and the Mo, Cu, and Ni cell voltages based on the Nernst equation (Eq. (22)) are given in Tables 2-4. Tests on O_2-Mo metal air batteries with oxygen from atmosphere typically yielded less than 10% efficiency. The accuracy of the weight determination was about 10 mg; so, a Mo-air battery reaction was eliminated.

In summary, the [MoCu (H permeation)/LiOH-LiBr/NiO] cell shown in Figure 3 ran for 65 hours before it was stopped for analysis, and produced 1.879 Wh compared to 1.078 Wh of input H_2O electrolysis energy and 0.355 Wh for 100% permeation H_2 conversion to H_2O corresponding to a net energy of 0.446 Wh (3.6 kJ). Fuel cells are typically less than 50% efficient; so, rather than considering 100% efficiency of electrolysis (0 ohmic loss) and 100% fuel cell reactions for electrolysis and permeation hydrogen as the maximum theoretical (1.433 Wh), a more realistic practical expectation is 0.143 Wh (0.516 kJ) corresponding to a net of 1.736 Wh of excess electricity. Other exotic reactions of the electrolyte or electrodes were also easily excluded as impossible to make electricity from H_2O as confirmed by the XRD analysis and experience in the fuel cell field such as that with molten alkaline, carbonate, and solid oxide fuel cells having Ni electrodes as discussed previously [2].

The power is expected to increase substantially with the use of high surface area materials. The CoCu tape cast-clad Ni permeable membrane anodes were very stable in LiOH-LiBr electrolyte and developed about 7.3 mW/cm^2. This comprises about a 35-fold improvement over the crushed Ni celmet anodes of our earlier results [2]. A very slight weight loss was observed that was likely due to loss of un-sintered powder since no visible signs of corrosion were detected by comparing the SEM of the pre- and post-run anode (Figures 4A-B) of cell [CoCu (H permeation)/LiOH-LiBr/NiO] that output 6.49 Wh, 150 mA, at 186% gain as shown in Table 5. These results demonstrate that the H_2 protection can be applied to high surface area materials as well. Given that the surface area of tape cast is orders of magnitude that of foils, and the power density was very significantly improved with surface area, a similar factor of beyond the 500 fold increase with Mo or Mo-alloy foil may be anticipated.

B. Spectroscopic Identification of Molecular Hydrino

MAS ^1H NMR, electron-beam excitation emission spectroscopy, Raman spectroscopy, and photoluminescence emission spectroscopy were performed on samples of reaction products comprising CIHT electrolyte, CIHT electrodes, and inorganic compound getter KCl-KOH mixture placed in the sealed container of closed CIHT cells.

MAS NMR of molecular hydrino trapped in a protic matrix represents a means to exploit the unique characteristics of molecular hydrino for its identification via its interaction with the matrix. A unique consideration regarding the NMR spectrum is the possible molecular hydrino quantum states. Similar to H_2 excited states, molecular hydrinos $H_2(1/p)$ have states with $\ell = 0,1,2,...,p-1$. Even the $\ell = 0$ quantum state has a relatively large quadrupole moment, and additionally, the corresponding orbital angular momentum of $\ell \neq 0$ states gives rise to a

magnetic moment [1] that could cause an upfield matrix shift. This effect is especially favored when the matrix comprises an exchangeable H such as a matrix having waters of hydration or an alkaline hydroxide solid matrix wherein a local interaction with $H_2(1/p)$ influences a larger population due to rapid exchange. CIHT cell getter KOH-KCl showed a shift of the MAS NMR active component of the matrix (KOH) from +4.4 ppm to about -4 to -5 ppm after exposure to the atmosphere inside of the sealed CIHT cell. For example, the MAS NMR spectrum of the initial KOH-KCl (1:1) getter, the same KOH-KCl (1:1) getter from CIHT cells comprising [MoNi/LiOH-LiBr/NiO] and [CoCu (H perm)/LiOH-LiBr/NiO] that output 2.5 Wh, 80 mA, at 125% gain, and 6.49 Wh, 150 mA, at 186% gain, respectively, (Figures 5A-C) showed that the known downfield peak of OH matrix shifted from about +4 ppm to the upfield region of about -4 ppm. Molecular hydrino produced by the CIHT cell shifted the matrix from positive to significantly upfield. The different ℓ quantum numbers possible for the p = 4 state can give rise to different upfield matrix shifts consistent with observations of multiple such peaks in the region of -4 ppm. The MAS NMR peak of the KOH matrix upfield shifted by forming a complex with molecular hydrino that can be sharp when the upfield shifted hydroxide ion (OH^-) acts as a free rotor, consistent with prior observations. The MAS-NMR results are consistent with prior positive ion ToF-SIMS spectra that showed multimer clusters of matrix compounds with di-hydrogen as part of the structure, $M:H_2$ (M = KOH or K_2CO_3). Specifically, the positive ion spectra of prior CIHT cell getters comprising KOH and K_2CO_3 such as of K_2CO_3-KCl (30:70 wt%) showed $K^+\left(H_2:KOH\right)_n$ and $K^+\left(H_2:K_2CO_3\right)_n$ consistent with $H_2(1/p)$ as a complex in the structure [2].

The direct identification of molecular hydrino by its characteristic extraordinarily high ro-vibrational energies was sought using Raman spectroscopy. Another distinguishing characteristic is that the selection rules for molecular hydrino are different from those of ordinary molecular hydrogen. Similar to H_2 excited states, molecular hydrinos have states with $\ell = 0,1,2,...,p-1$ wherein the prolate spheroidal photon fields of $H_2(1/p)$; $p =$ 1, 2, 3,...,137 have spherical harmonic angular components of quantum number ℓ relative to the semimajor axis [1]. Transitions between these prolate spheroidal harmonic states are permissive of rotational transitions of $\Delta J = 0, \pm 1$ during a pure vibrational transition without an electronic transition as observed for H_2 excited states. The lifetimes of the angular states are sufficiently long such that $H_2(1/p)$ may uniquely undergo a pure ro-vibrational transition having the selection rule $\Delta J = 0, \pm 1$.

The emitting ro-vibrational molecular hydrino state may be excited by a high-energy electron collision or by a laser wherein due to the rotational energy of $p^2(J+1)0.01509\ eV$ [1], excited rotational states cannot be populated as a statistical thermodynamic population at

ambient temperatures since the corresponding thermal energy is less than 0.02 eV. Thus, the ro-vibrational state population distribution reflects the excitation probability of the external source. Moreover, due to the thirty-five times higher vibrational energy of $p^2 0.515\, eV$ over the rotational energy, only the first level, $\upsilon = 1$, is expected to be excited by the external source. Molecular hydrino states can undergo ℓ quantum number changes at ambient temperature, and the J quantum state may be changed during e-beam or laser irradiation as the power is thermalized. The initial state may be any one of $\ell = 0,1,2,3$ independently of the J quantum number. Thus, rotational and ro-vibrational transitions are Raman and IR active with the R, Q, P branches being allowed wherein the angular momentum is conserved between the rotational and electronic state changes. Permitted by the change in ℓ quantum number, the de-excitation vibrational transition $\upsilon = 1 \to \upsilon = 0$ with a rotational energy up conversion ($J' - J'' = -1$), a down conversion ($J' - J'' = +1$), and no change ($J' - J'' = 0$) gives rise to the P, R, and Q branches, respectively. The Q-branch peak corresponding to the pure vibrational transition $\upsilon = 1 \to \upsilon = 0;\ \Delta J = 0$ is predicted to be the most intense with a rapid decrease in intensity for the P and R series of transition peaks of higher order. Due to the available energy of internal conversion, more peaks of higher intensity are expected for the P branch relative to the R branch. An influence of the matrix is expected to cause a vibrational energy shift from that of a free vibrator, and a matrix rotational energy barrier is anticipated to give rise to about the same energy shift to each of the P and R branch peaks, manifested as a nonzero intercept of the linear energy separation of the series of rotational peaks.

It was reported previously [2] that ro-vibrational emission of $H_2(1/4)$ trapped in the crystalline lattice of getters of CIHT cell gas was excited by an incident 6 KeV electron gun with a beam current of 8 μA in the pressure range of 5 X 10^{-6} Torr, and recorded by windowless UV spectroscopy. By the same method $H_2(1/4)$ trapped in the metal crystalline lattice of MoCu was observed by electron-beam excitation emission spectroscopy. An example of the resolved ro-vibrational spectrum of $H_2(1/4)$ (the so called 260 nm band) recorded from the MoCu anode of the CIHT cell [MoCu(50/50) (H permeation)/LiOH+LiBr/NiO] that output 5.97 Wh, 80 mA, at 190% gain shows the peak maximum at 258 nm (Figure 6) with representative positions of the peaks at 227, 238, 250, 263, 277, and 293 nm, having an equal spacing of 0.2491 eV. The results are in very good agreement with the predicted values for $H_2(1/4)$ for the transitions of the matrix-shifted vibrational and free rotor rotational transitions of $\upsilon = 1 \to \upsilon = 0$ and Q(0), R(0), R(1), P(1), P(2), and P(3), respectively, [2] wherein Q(0) is identifiable as the most intense peak of the series. The peak width (FWHM) was 4 nm. Broadening of ro-vibrational transitions of $H_2(1/4)$ relative to ordinary H_2 in a crystalline lattice is expected since the energies involved are extraordinary, being sixteen times higher, and significantly couple to phonon bands of the lattice

resulting in resonance broadening. The 260 nm band was not observed on the MoCu starting material. The 260 nm band was observed as a second order Raman fluorescence spectrum from KOH-KCl crystals that served as a getter of $H_2(1/4)$ gas when sealed in CIHT cells as described previously [2] and shown in Figures 11A-D. The 260 nm band was also observed on the CoCu anode.

$H_2(1/4)$ was further confirmed using Raman spectroscopy wherein due to the large energy difference between ortho and para, the latter was expected to dominate the population. Given that para is even, the typical selection rule for pure rotational transitions is $\Delta J = \pm 2$ for even integers. However, orbital-rotational angular momentum coupling gives rise to a change in the ℓ quantum number with the conservation of the angular momentum of the photon that excites the rotational level wherein the resonant photon energy is shifted in frequency by the orbital-nuclear hyperfine energy relative to the transition in the absence of the ℓ quantum number change. Moreover, for $\ell \neq 0$, the nuclei are aligned along the internuclear axis as given in Chp 12 of Ref. [1]. The rotational selection rule for Stokes spectra defined as initial state minus final state is $\Delta J = J' - J'' = -1$, the orbital angular momentum selection rule is $\Delta \ell = \pm 1$, and the transition becomes allowed by the conservation of angular momentum during the coupling of the rotational and the orbital angular momentum excitations [1]. And, no intensity dependency on nuclear spin is expected.

Using a Thermo Scientific DXR SmartRaman with a 780 nm diode laser in the macro mode, a 40 cm^{-1} broad absorption peak was observed on MoCu hydrogen permeation anodes after the production of excess electricity (Figures 7A-D). The peak was not observed in the virgin alloy (Figure 7A), and the peak intensity increased with increasing excess energy and laser intensity. Moreover it was present pre and post sonication (Figures 7B-C) indicating that the only possible elements to consider as the source were Mo, Cu, H, and O as confirmed by SEM-EDX. Permutations of control compounds did not reproduce the peak. The peak was also observed on cells having Mo, CoCu, and MoNiAl anodes such as the cell [CoCu (H permeation)/LiOH-LiBr/NiO] that output 6.49 Wh, 150 mA, at 186% gain and the cell [MoNiAl (45.5/45.5/9 wt%)/LiOH-LiBr/NiO] that output 2.40 Wh, 80 mA, at 176% gain as shown in Figures 7E and 7F, respectively. In separate experiments, KOH-KCl gettered gas from these cells gave a very intense fluorescence or photoluminescence series of peaks that were assigned to $H_2(1/4)$ ro-vibration (Figures 11A-D). Since no other element or compound is known that can absorb a single 40 cm^{-1} (0.005 eV) near infrared line at 1.33 eV (the energy of the 780 nm laser minus 2000 cm^{-1}), $H_2(1/4)$ was considered. The absorption peak starting at 1950 cm^{-1} (Figures 7B-E) matched the free space rotational energy of $H_2(1/4)$ (0.2414 eV) to four significant figures, and the width of 40 cm^{-1} matches the orbital-nuclear coupling energy splitting [1].

The absorption peak matching the $H_2(1/4)$ rotational energy is a real peak and cannot be explained by any known species. The excitation of the hydrino rotation may cause the absorption peak by two mechanisms. In the first, the Stokes light is absorbed by the lattice due to a strong interaction of the rotating hydrino as a lattice inclusion. This is akin to resonance broadening observed with the 260 nm e-beam band [2]. The second comprises a known inverse Raman effect [8]. Here, the continuum caused by the laser is absorbed and shifted to the laser frequency wherein the continuum is strong enough to maintain the rotational excited state population to permit the antiStokes energy contribution. Typically, the laser power is very high for an IRE, but molecular hydrino may be a special case due to its non-zero ℓ quantum number and corresponding selections rules. Moreover, MoCu, is anticipated to cause Surface Enhanced Raman Scattering (SERS) mixture of metals. So, the results are discussed from the context of the latter mechanism.

The absorption was assigned to an inverse Raman effect (IRE) [8] for the $H_2(1/4)$ rotational energy for the $J' = 1$ to $J'' = 0$ transition [1]. This result shows that $H_2(1/4)$ is a free rotor which is the case with H_2 in a silicon matrix [7]. Moreover, since $H_2(1/4)$ may form complexes with hydroxide as shown by MAS NMR and ToF-SIMs [2], and a matrix shift is observed with the electron-beam excitation emission spectrum and the photoluminescence spectrum [2] due to the influence of the local environment at the $H_2(1/4)$ site in the lattice, the IRE is anticipated to shift as well in different matrices and also with pressure. Likewise, the Raman peaks of H_2 as a matrix inclusion shift with pressure [7]. Several instances were observed by Raman spectral screening of metals and inorganic compounds. Ti and Nb showed a small absorption peak of about 20 counts starting at 1950 cm^{-1}. Al showed a much larger peak as shown in Figure 7G. Instances of inorganic compounds included LiOH and LiOH-LiBr (Figures 7H-J) that showed the peak at 2308 cm^{-1} and 2608 cm^{-1}, respectively. Ball milling LiOH-LiBr caused a reaction to greatly intensify the IRE peak and shift it to be centered at 2308 cm^{-1} like LiOH as well as form a peak centered at 1990 cm^{-1}. An especially strong absorption peak was observed at 2447 cm^{-1} from $Ca(OH)_2$ (Figure 7K) that forms H_2O. The latter may serve as a catalyst to form $H_2(1/4)$ upon dehydration of $Ca(OH)_2$ at 512 °C or by reaction with CO_2. These are solid fuel type reactions to form hydrinos as reported previously [2]. LiOH and $Ca(OH)_2$ both showed a $H_2(1/4)$ IRE peak, and the LiOH is commercially formed from $Ca(OH)_2$ by reaction with Li_2CO_3. Thus, $Ca(OH)_2 + Li_2CO_3$ mixture was caused to react by ball milling, and a very intense $H_2(1/4)$ IRE peak was observed centered at 1997 cm^{-1} (Figure 7L).

$H_2(1/4)$ as the product of solid fuel reactions was reported previously [2-4]. The energy released by forming hydrinos according to Eqs. (1-4) was shown to give rise to high kinetic energy H^-. Using solid fuel Li + $LiNH_2$ + dissociator Ru-Al_2O_3 that can form H and HOH catalyst by decomposition of $Al(OH)_3$ and reaction of Li with H_2O and $LiNH_2$, ions arriving

before m/e = 1 were observed by ToF-SIMS (Figure 8) that confirmed the energy release of Eq. (4) is manifest as high kinetic energy H^-. Other ions such as oxygen (m/e = 16) showed no early peak. The relation between time of flight T, mass m, and acceleration voltage V is

$$T = A\sqrt{\frac{m}{V}} \tag{18}$$

where A is a constant that depends on ion flight distance. From the early peak in Figure 8 at m/e = 0.968 with an acceleration voltage of 3 kV, the kinetic energy imparted to the H species from the hydrino reaction is about 204 eV, which is a match to the HOH catalyst reaction given by Eqs. (1-4). The same early spectrum was observed in the positive mode corresponding to H^+, but the intensity was lower.

XPS was performed on the solid fuel [3]. The XPS of LiHBr formed by the reaction of Li, LiBr, $LiNH_2$, dissociator R-Ni (comprising about 2wt% $Al(OH)_3$), and 1 atm H_2, shows a peak at 494.5 eV and 495.6 eV for XPS spectra on reaction products of two different runs (Figures 9A and9B) that could not be assigned to any known elements. Na, Sn, and Zn being the only possibilities were easy to eliminate based on the absence of any other corresponding peaks of these elements since only Li, Br, C, and O peaks were observed. The peak matched the energy of the theoretically allowed double ionization [2] of molecular hydrino $H_2(1/4)$. Molecular hydrino was further confirmed as a product by Raman and FTIR spectroscopy. The Raman spectrum of solid fuel product LiHBr (Figure 7M) shows a $H_2(1/4)$ inverse Raman effect absorption peak centered at 1994 cm^{-1}. The FTIR spectrum of solid fuel product LiHBr (Figure 10) shows a new sharp peak at 1988 cm^{-1} that is a close match to the free rotor energy of $H_2(1/4)$. Furthermore, the MAS NMR showed a strong up-field shift peak [3] consistent with that shown in Figures 5B and 5C.

XPS was also performed on the anodes of CIHT cells such as [MoCu (H permeation)/LiOH-LiBr/NiO] (1.56 Wh, 50 mA, at 189% gain), and [MoNi (H permeation)/LiOH-LiBr/NiO] (1.53 Wh, 50 mA, at 190%) as shown in Figures 9C and 9D. The 496 eV peak was observed as well. The peak was assigned to $H_2(1/4)$ since the other possibilities were eliminated. Specifically, in each case, the 496 eV peak could not be associated with Mo 1s, as its intensity would be much smaller than Mo 3p peaks and the energy would be higher than that observed, and it could not be assigned to Na KLL, since there is no Na 1s in the spectrum.

Another successful cross-confirmatory technique in the search for hydrino spectra involved the use of the Raman spectrometer wherein the ro-vibration of $H_2(1/4)$ matching the 260 nm e-beam band was observed as second order fluorescence. The gas from the cells [Mo, 10 bipolar plates/LiOH-LiBr-MgO/NiO] (2550.5 Wh, 1.7A, 9.5V, at 234% gain), [MoCu/LiOH-LiBr/NiO] (3.5 Wh, 80 mA, at 120% gain), [MoNi/LiOH-LiBr/NiO] (1.8 Wh, 80 mA, at 140%

gain) was gettered with KOH-KCl (50-50 at%), and [CoCu (H permeation)/LiOH-LiBr/NiO] (6.49 Wh, 150 mA, at 186% gain), and the Raman spectra were recorded on the getters using the Horiba Jobin Yvon LabRAM Aramis Raman spectrometer with a HeCd 325 nm laser in microscope mode with a magnification of 40X. In each case, an intense series of 1000 cm^{-1} (0.1234 eV) equal-energy spaced Raman peaks (Figures 11A-D) were observed in the 8000 cm^{-1} to 18,000 cm^{-1} region. The conversion of the Raman spectrum into the fluorescence or photoluminescence spectrum revealed a match as the second order ro-vibrational spectrum of $H_2(1/4)$ corresponding to the 260 nm band first observed by e-beam excitation [2]. The peak assignments to the Q, R, and P branches for the spectra shown in Figures (11A-D) are Q(0), R(0), R(1), R(2), R(3), R(4), P(1), P(2), P(3), P(4), P(5), and P(6) observed at 13,183, 12,199, 11,207, 10,191, 9141, 8100, 14,168, 15,121, 16,064, 16,993, and 17,892 cm^{-1}, respectively. The excitation was deemed to be by the high-energy UV and EUV He and Cd emission of the laser wherein the laser optics are transparent to at least 170 nm and the grating (Labram Aramis 2400g/mm 460mm focal length system with 1024 X 26 μm^2 pixels CCD) is dispersive and has its maximum efficiency at the shorter wavelength side of the spectral range, the same range as the 260 nm band. For example, cadmium has a very intense line at 214.4 nm (5.8 eV) that matches the ro-vibrational excitation energy of $H_2(1/4)$ in KCl matrix based on the e-beam excitation data [9]. The CCD is also most responsive at 500 nm, the region of the second order of the 260 nm band centered at 520 nm.

The photoluminescence bands shown in Figures 11C and 11D were also correlated with the upfield shifted NMR peaks. For example, the KOH-KCl (1:1) getter from MoNi anode CIHT cells comprising [MoNi/LiOH-LiBr/NiO] having upfield shifted matrix peaks at -4.04 and -4.38 ppm (Figure 5B) and the KOH-KCl (1:1) getter from CoCu H permeation anode CIHT cells comprising [CoCu (H permeation)/LiOH-LiBr/NiO] having upfield shifted matrix peaks at -4.09 and -4.34 ppm (Figure 5C) showed the series of photoluminescence peaks corresponding to the 260 nm e-beam.

Overall, the Raman results such as the observation of the 0.241 eV (1940 cm^{-1}) Raman inverse Raman effect peak and the 0.2414 eV-spaced Raman photoluminescence band that matched the 260 nm e-beam spectrum is strong confirmation of the presence of a molecular hydrino having an internuclear distance that is 1/4 that of H_2. The evidence in the latter case is further substantiated by being in a region having no known first order peaks or possible assignment of matrix peaks at four significant figure agreement with theoretical predictions.

IV. Conclusion

Open CIHT cells comprising Mo or Mo alloy hydrogen permeable anodes, a NiO cathode, and a LiOH-LiBr-MgO electrolyte, operated continuously and with enough stability to produce electricity at commercial power densities until stopped for analysis. The CIHT cells showed significantly more electrical energy output than their input and generated hydrogen fuel from H_2O. Each cell ran off of H_2O vapor from which hydrogen and oxygen were generated by intermittent electrolysis and supplied to the electrochemical process of the cell. However, hydrogen was added to the anode for a time to achieve a steady state between consumption and that formed by electrolysis. Operating at a negative voltage relative to the thermodynamic anode corrosion voltage and in the presence of hydrogen supplied to the anode through the hydrogen permeable membrane, hydrogen was found to stabilize the anode to corrosion. Due to the electrochemistry occurring in the cell, an electrical current flowed through a load of the electrical testing instrument with an internal ion flow of the ionic-conductive electrolyte, completing the electrical circuit. The two currents were indicative of forming hydrinos as the only identifiable source of the gain in electrical capacity and energy. This conclusion was supported by the absence of any possible known source of electricity based on the corresponding energy and mass balance. The predicted molecular hydrino $H_2(1/4)$ was identified as a product of CIHT cells by MAS ^1H NMR, electron-beam excitation emission spectroscopy, Raman spectroscopy, XPS, and photoluminescence emission spectroscopy.

Based on industry experience, a Mo-Ni anode can be stabilized with H_2 flow. The power of a >1-yr stable anode in a MCFC operating at a higher temperature [10] is up to 100 mW/cm^2. The lesser kinetically favorable anode material Co-Cu (82-18 wt%) was protected from corrosion by cladding a tape cast onto a hydrogen permeable Ni membrane to achieve comparable power densities as Mo and MoCu foils due to the large surface area of the tape cast. Much higher power densities are anticipated with the use of high-surface area Mo and Mo alloy materials. CIHT cell Mo-based anodes can support >100 mW/cm^2 power density from the hydrino reaction without considering the improvement in power density from using high surface area materials versus foil. Typically, electrical power generated from permeation H is about 100% of the maximum versus the practical fuel cell efficiency of <50% due to a hydrino contribution; so, 100 mW/cm^2 excess electricity over permeation is predicted at the most conservative H_2 flow to achieve anode stability. Electrolysis is essentially 100%, and the H_2 pressure of the H permeable anode achieves steady state from the electrolysis such that the cell requires no further external H consumption; so, achieving the absence of corrosion by H_2 protection should be readily achievable. Moreover, a matrix separator such as MgO should further be protective. Another option is to electroplate any Mo loss since the corrosion product is soluble in the electrolyte,

unlike the case with NiO wherein a Ni anode was shown to not be regenerable. MoO_2 or Li_2MoO_4 can be added to the electrolyte to force some continuous electroplating to balance any lost by corrosion. Experimentally the cell comprising [MoCu (H permeation)/LiOH-LiBr/NiO] was intentionally degraded and subsequent long duration operation (~ 21 days) was achieved equivalent to the initial results by electroplating added MoO_2 at 1.2V for 6 hrs.

The CIHT cell has attributes for being very commercially competitive. The cell was continuously regenerative and operated at essentially instantaneous steady power output during discharge over long duration as shown by the plot of discharge energy with time (Figure 3). In power applications, a portion of a stack could provide electrolysis power for another and the thermal losses are calculated to be 1% or less such that the system is standalone [11]. The CIHT cell operated under conditions that were similar to those of existing technology such as batteries and fuel cells, but used abundant, nontoxic, commodity chemicals that project a factor of at least 10 fold reduction in capital costs relative to conventional electricity sources. Unlike conventional batteries, the CIHT cell does not need to be recharged externally, and unlike a fuel cell, the CIHT cell is charged, but creates an amplification of the charge by converting H_2O to hydrino at an extraordinary energy release of 50 MJ/mole H_2O, about 200 times the energy of the combustion reaction of conventional fuel cells. Due to the high energy yield and unique fuel and products H_2O and O_2 with $H_2(1/4)$, respectively, the conventional gas manifolds and channel plates of fuel cells may be eliminated. H_2 may be initially supplied to a H_2 permeable membrane anode until steady state is achieved. Thereafter, the mass balance is reduced to H_2O input with O_2 output at the cathode wherein the latter is a positive feature and $H_2(1/4)$ at the anode. Moreover, hydrinos easily diffuse from the cell. Engineering calculations show that a 20 μm porous cathode can support 100 mA/cm^2 from the hydrino reaction with 25 cm diameter plates [12]. Considering the range of surface power densities with dimensions of 10 μm, 10 μm, and 20 μm for the anode, the electrolyte layer, and the porous cathode to provide H_2O transport to the reaction, volumetric power densities of 2.5 kW/liter and 25 kW/liter are feasible having a corresponding material cost of about $70/kW and $7/kW (Table 6), respectively.

The continuous autonomous generation of electricity from H_2O was achieved by a safe, nonpolluting, simple, reliable, sustainable, and inexpensive system operating under standard conditions. The CIHT cell that directly converts H_2O into electricity, molecular hydrino (the dark matter of the universe [1, 13]), and oxygen could be transformational to the energy industry, freeing electrical power, electric motive power, and electric propulsion from any grid or fuels infrastructure.

References

1. R. Mills, *The Grand Unified Theory of Classical Physics*; 2014 Edition, posted at http://www.blacklightpower.com/theory/bookdownload.shtml.
2. R. Mills , X Yu, Y. Lu, G Chu, J. He, J. Lotoski, "Catalyst induced hydrino transition (CIHT) electrochemical cell," Int. J. Energy Res., published online December 20, 2013, 25 pages, doi: 10.1002/er.3142.
3. R. L. Mills, G. Zhao, K. Akhtar, Z. Chang, J. He, Y. Lu, W. Good, G. Chu, B. Dhandapani, "Commercializable Power Source from Forming New States of Hydrogen," Int. J. Hydrogen Energy, Vol. 34, (2009), 573–614.
4. R. L. Mills, G. Zhao, K. Akhtar, Z. Chang, J. He, X. Hu, G. Wu, J. Lotoski, G. Chu, "Thermally reversible hydrino catalyst systems as a new power source," Int. J. Green Energy, Vol. 8 (2011), pp. 429–473.
5. R. L. Mills, M. Nansteel, W. Good, G. Zhao, "Design for a BlackLight Power multi-cell thermally coupled reactor based on hydrogen catalyst systems," International Journal of Energy Research, Vol. 35, (2011).
6. R. L. Mills, G. Zhao, W. Good, "Continuous thermal power system," Applied Energy, Vol. 88, (2011), pp. 789–798, doi: 10.1016/j.apenergy.2010.08.024.
7. E. E. Chen, M. Stavola, W. B. Fowler, J. A. Zhou, "Rotation of Molecular Hydrogen in Si: Unambiguous Identification of Ortho-H_2 and Para-D_2," Phys. Rev. Letts., 88(24), (2002), pp. 245503-1 to 245503-4.
8. W. J. Jones, B. P. Stoicheff, "Inverse Raman spectra: Induced absorption at optical frequencies," Physical Review Letters, Vol. 13, No. 22, (1964), pp. 657-659.
9. http://physics.nist.gov/PhysRefData/Handbook/Tables/cadmiumtable2.htm.
10. K. Hatoh, J. Niikura, E. Yasumoto, T. Gamo, "Molten carbonate fuel cell", US Patent No: 5,354,627, Matsushita Electric Industrial Co., Ltd, Oct. 11, 1994.
11. M. Nansteel, "Thermal Analysis of CIHT Cells", BlackLight Power Technical Report, March, 15, 2012.
12. M. Nansteel, "Water Vapor Transport in the CIHT Cell Porous Cathode", BlackLight Power Technical Report, October 8, 2012.
13. R. L. Mills, Y. Lu, "Hydrino continuum transitions with cutoffs at 22.8 nm and 10.1 nm," Int. J. Hydrogen Energy, Vol. 35, (2010), pp. 8446-8456, doi: 10.1016/j.ijhydene.2010.05.098.
14. O. Knacke, O. Kubascheeski, K. Hesselmann, *Thermochemical Properties of Inorganic Substances*, 2nd Ed., Springer-Verlag Berlin, Heidelberg 1991.

Table 1. CIHT hydrogen permeation cell comprising a molten LiOH-LiBr electrolyte: [MoCu/LiOHLiBr/NiO].

Cell Type	H_2 Permeation
Anode	MoCu .02in foil (Ametek OD 3.8cm, 11g) disk with Ni seam weld to matching piece; with top side center welded 0.25" nickel gas line, net top disk surface area 11cm^2, submerged
Cathode	Pre-oxidized porous Ni CNi6 (ID 1.2cm, OD 3.8cm, 5cm tall), on top of electrolyte
Electrolyte	15.0 g LiOH + 75.0 g LiBr
Temperature	430 ^oC
Atm Type	Open to atmosphere (20.9% O_2)
Open Circuit Voltage	1.07 V
Pressure Range	930–980 torr
Program Charge	1s, 50mA
Program Discharge	2s, 50mA
Longest Run Time	65 hours
Voltage Range at 65 hours	0.96–1.02V steady
Largest Instantaneous Gain	1.76 X
Cumulative Net Gain	1.76 X
Cumulative Discharge Energy	1.879 Whr
Cumulative Charge Energy	1.078 Whr
Cumulative Net Energy	0.801 Whr
Cell Power	49.56 mW
Area Power Density	4.23 mW/cm^2
Amount of H_2 consumed	2.83 x 10^{-3} moles
H_2 Permeation Rate	2.62 x 10^{-8} mol/sec
Maximum Energy Contribution from H_2	0.355 Whr
Power from H_2	5.35 mW
Area Power Density of H_2	0.504 mW/cm^2
Overall Hydrino Energy Contribution	0.446 Whr

Table 2. Thermodynamic parameters of the reaction of molybdenum metal with O_2 at 700 K [14].

Reaction	$Mo + 1.5O_2$ to MoO_3		
	Mo	O_2	MoO_3
Stoichiometry	1	1.5	1
HoF @ 700 K (kJ/mol)	10.451	12.552	-710.038
S @ 700 K (J/molK)	50.604	231.579	150.836
δH (kJ/mol)	10.451	18.828	-710.038
δG (kJ/mol)	-30.032	-259.067	-830.707
δHrxn (kJ/mol)	-733.041		
δGrxn (kJ/mol)	-541.608		
T (K)	700		
n	6		
E° (700K)	0.936	Volts	

Table 3. Thermodynamic parameters of the reaction of copper metal with O_2 at 700 K [14].

Reaction	$Cu + (1/2)O_2$ to CuO		
	Cu	O_2	CuO
Stoichiometry	1	0.5	1
HoF @ 700 K (kJ/mol)	10.275	12.552	-136.507
S @ 700 K (J/molK)	54.858	231.579	83.544
δH (kJ/mol)	10.275	6.276	-136.507
δG (kJ/mol)	-33.611	-86.356	-203.342
δHrxn (kJ/mol)	-159.334		
δGrxn (kJ/mol)	-83.375		
T (K)	700		
n	2		
E° (700K)	0.432	Volts	

Table 4. Thermodynamic parameters of the reaction of nickel metal with O_2 at 700 K [14].

Reaction	Ni + (1/2)O_2 to NiO		
	Ni	O_2	NiO
Stoichiometry	1	0.5	1
HoF @ 700 K (kJ/mol)	12.351	12.552	-217.867
S @ 700 K (J/molK)	55.603	231.579	83.868
δH (kJ/mol)	12.351	6.276	-217.867
δG (kJ/mol)	-32.131	-86.356	-284.961
δHrxn (kJ/mol)	-242.770		
δGrxn (kJ/mol)	-166.474		
T (K)	700		
n	2		
E° (700K)	0.863	Volts	

Table 5. CIHT hydrogen permeation cell comprising a molten LiOH-LiBr electrolyte: [CoCu (H permeation)/LiOHLiBr/NiO].

Cell Type	H_2 Permeation protective tape casting CIHT cell
Anode	3 Pieces Co-Cu tape casting circle (OD 3.8cm) cladding with Ni permeation disk (OD 2.3 cm, 0.010" thickness) with top side center welded 0.25" nickel tube, net top disk surface area 11cm^2
Cathode	Lithiated pre-oxidized porous Ni CNi6 (ID 1.2cm, OD 5.7cm, 7.5cm tall), ~ 1 cm submerged into the electrolyte
Electrolyte	35.0 g LiOH + 175.0 g LiBr
Temperature	420 ^oC
Atm Type	Open to atmosphere (20.9% O_2)
Open Circuit Voltage	0.85 V
Pressure Range	870-900 torr
Program Charge	0.2s, 150mA
Program Discharge	0.4s, 150mA
Longest Run Time	96 hours
Voltage Range at 65 hours	0.73V
Largest Instantaneous Gain	1.83 X
Cumulative Net Gain	1.86 X
Cumulative Discharge Energy	6.49 Whr
Cumulative Charge Energy	3.49 Whr
Cumulative Net Energy	3.00 Whr
Cell Power	82.3 mW
Area Power Density	7.28 mW/cm^2
Amount of H_2 consumed	1.28 x 10^{-2} moles
H_2 Permeation Rate	2.65 x 10^{-7} mol/min*cm^2
Maximum Energy Contribution from H2	0.64 Whr
Anode weight loss after running	0.10 g
Maximum Energy Contribution anode weight lost	0.08 Whr
Overall Hydrino Energy Contribution	2.28 Whr

Table 6. Estimate of cost per kWatt electric of CIHT cell [Mo/LiOH-LiBr-MgO/NiO].

-Anode: 10 μm Mo foil.

-Cathode: 20 μm in situ oxidized NiO.

-Electrolyte: 10 μm LiOH-LiBr-MgO (1-5-2).

Cell Component	Volume per kW (cm^3)	Density (g/cm^3)	Weight per kW (g)	Cost ($/g)	Component Cost [a] ($/kW)
Cathode	11.85	8.91	105.6	0.02	1.81
Anode	10.00	12.28	122.8	0.04	4.99
Electrolyte:					
LiOH	2.55	1.46	3.72	0.01	0.04
LiBr	5.37	3.46	18.6	0.01	0.19
MgO	2.08	3.58	7.45	0.01	0.07
				Total	**7.10**

[a] Sources. Cathode: LME, average of three most recent months seller's price; Anode: MetalsPrices.com average of two most recent months high price molybdenum-98-00-99-95-China; Electrolyte: Manufacturers' prices from their websites or quotes.

Figure 1. CIHT cell schematic.

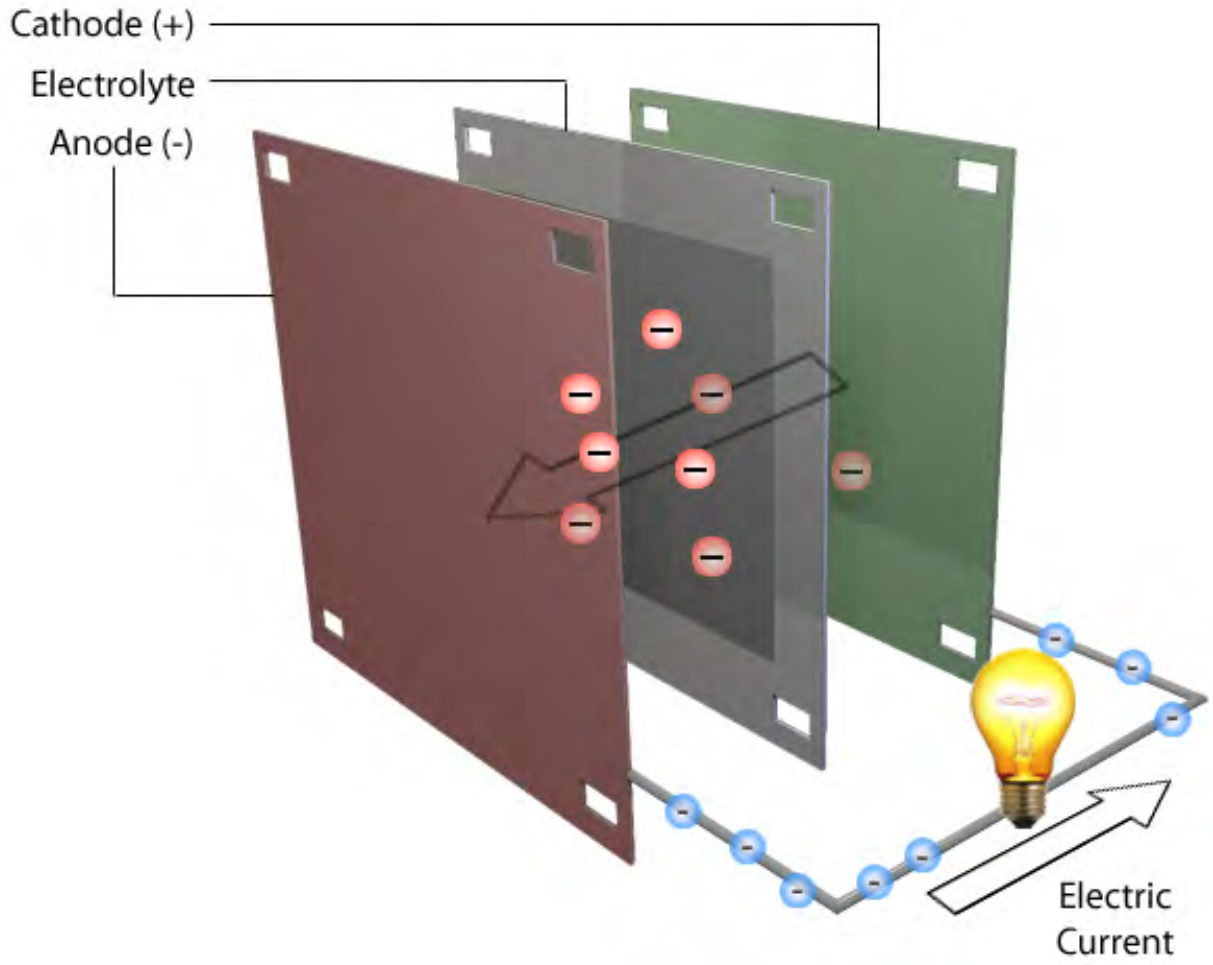

Figure 2. Representative charge and discharge voltage and current over time of the CIHT cell [MoCu/LiOH-LiBr/NiO] of Table 1 recorded with the digital oscilloscope. A. Captured and processed data. B. Screen shot.

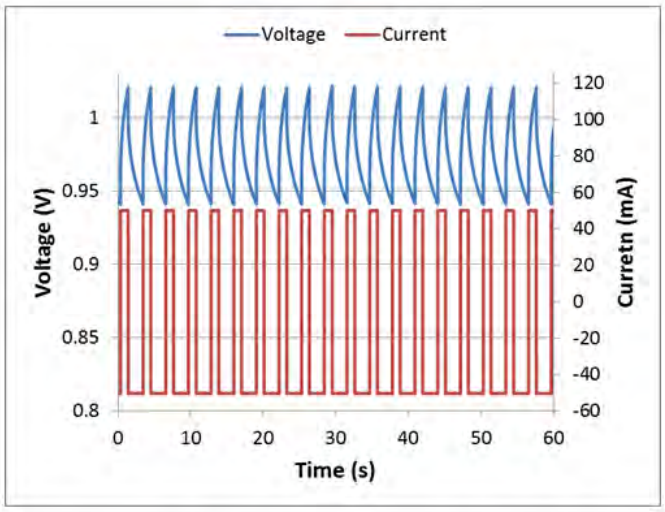

A

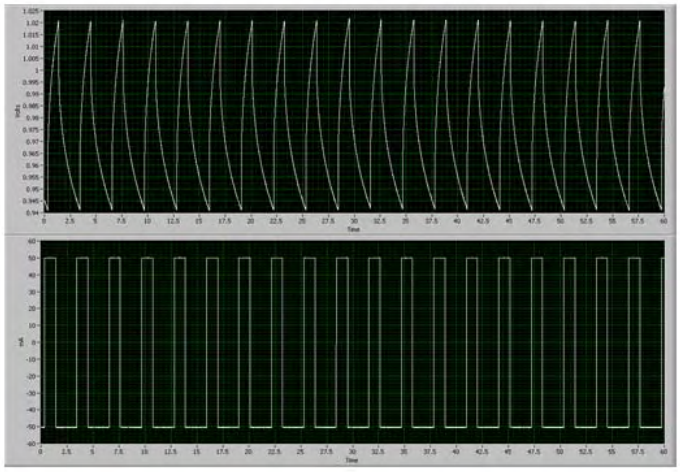

B

Figure 3 A–B. The charge and discharge voltages, and accumulated electrical charge and discharge energies over time of the CIHT cell [MoCu/LiOH-LiBr/NiO] of Table 1. A. Captured and processed data. B. Arbin screen shot.

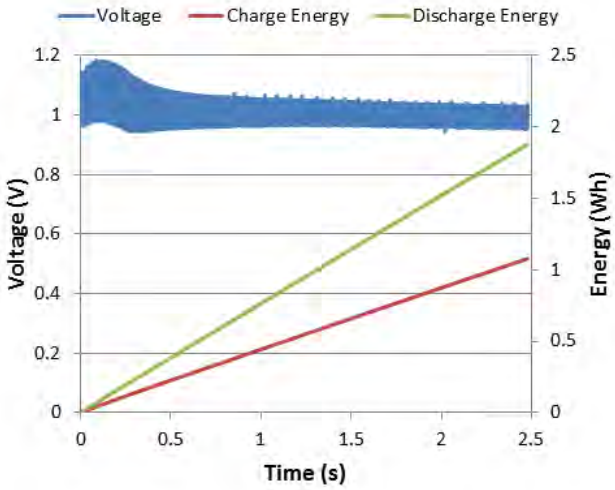

A

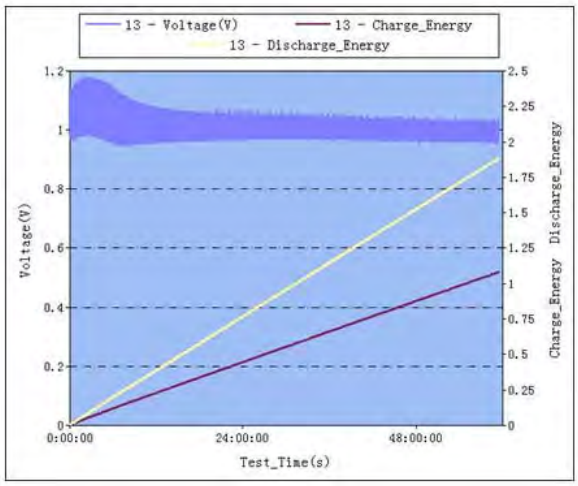

B

Figures 4A-B. Pre- and post-SEM of the anode of the CIHT cell comprising [CoCu (H permeation)/LiOH-LiBr/NiO] that output 6.49 Wh, 150 mA, at 186% gain. A. Prerun. B. Postrun. EDX showed that the material had a uniform Cu and Co distribution, and the SEM image showed fine, smooth metallic features suggesting the formation of an alloy.

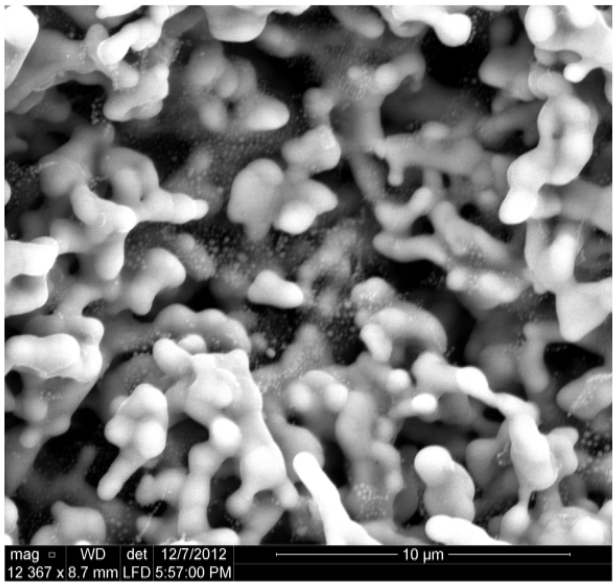

A

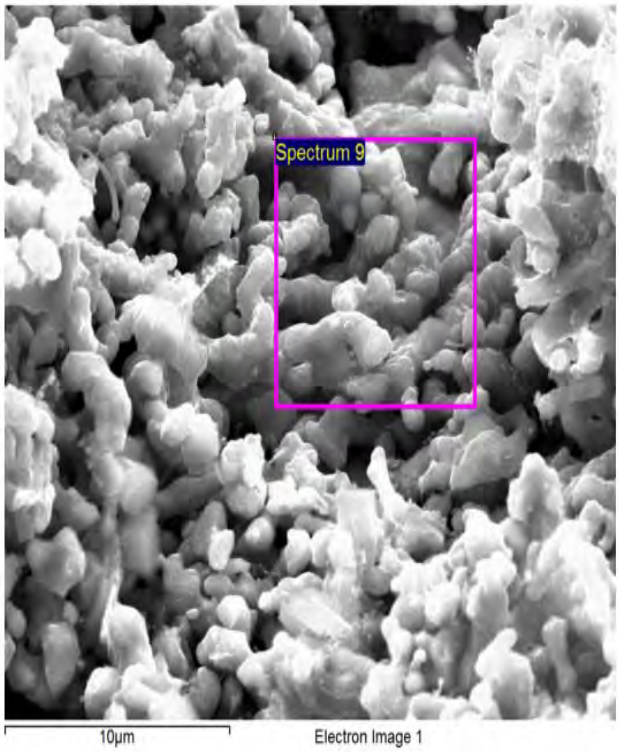

B

Figures 5A-C. ^{1}H MAS NMR spectra relative to external TMS. A. The initial KOH-KCl (1:1) getter that shows the known down-field shifted matrix peak at +4.44 ppm. B. The KOH-KCl (1:1) getter from a CIHT cell comprising [Mo/LiOH-LiBr/NiO] that output 2.5 Wh, 80 mA, at 125% gain that shows upfield shifted matrix peaks at -4.04 and -4.38 ppm. The symmetrically spaced peaks are spinning side bands. C. The KOH-KCl (1:1) getter from a CIHT cell comprising [CoCu (H permeation)/LiOH-LiBr/NiO] that output 6.49 Wh, 150 mA, at 186% gain that shows upfield shifted matrix peaks at -4.09 and -4.34 ppm. The symmetrically spaced peaks are spinning side bands.

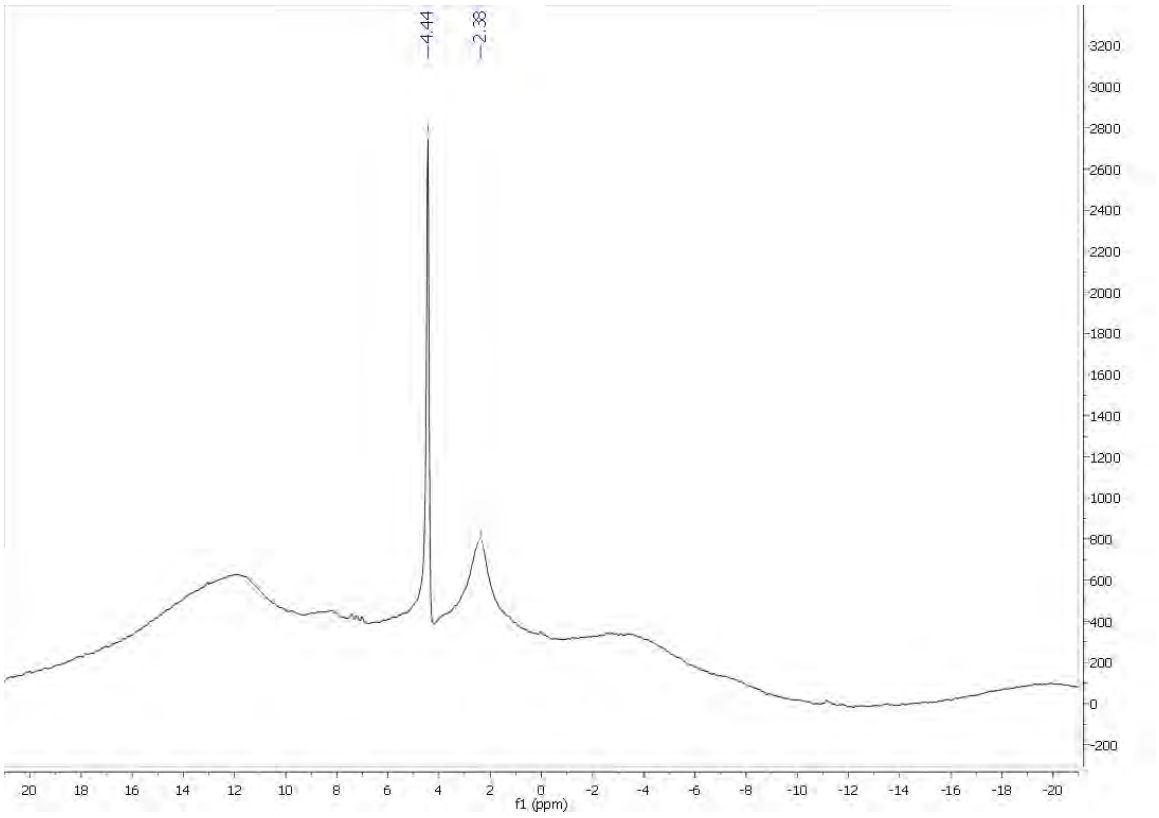

A

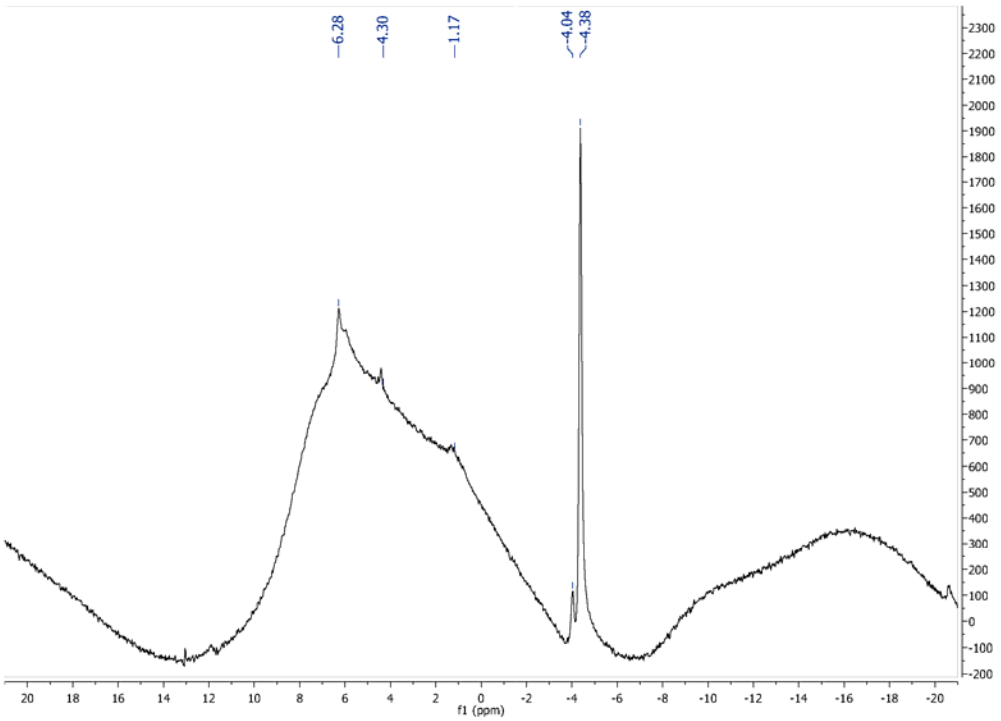

B

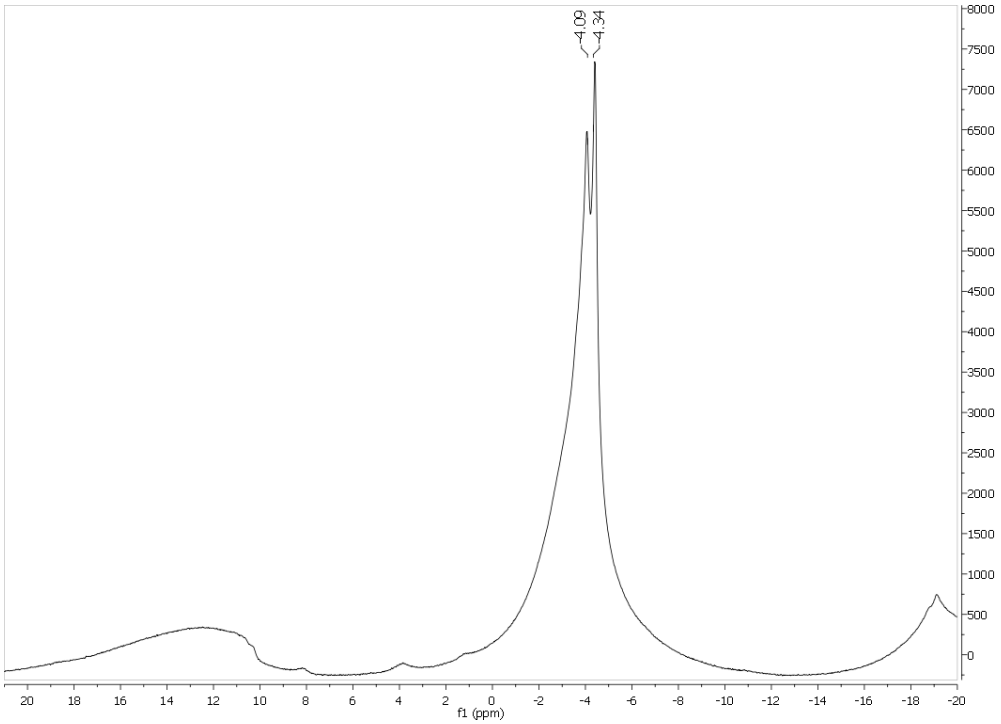

C

Figure 6. The electron-beam excitation emission spectrum recorded on the MoCu anode of the CIHT cell [MoCu(50/50) (H permeation)/LiOH+LiBr/NiO] that output 5.97 Wh, 80 mA, at 190% gain showing the 260 nm band comprising the peaks Q(0), R(0), R(1), P(1), P(2), and P(3) of $H_2(1/4)$.

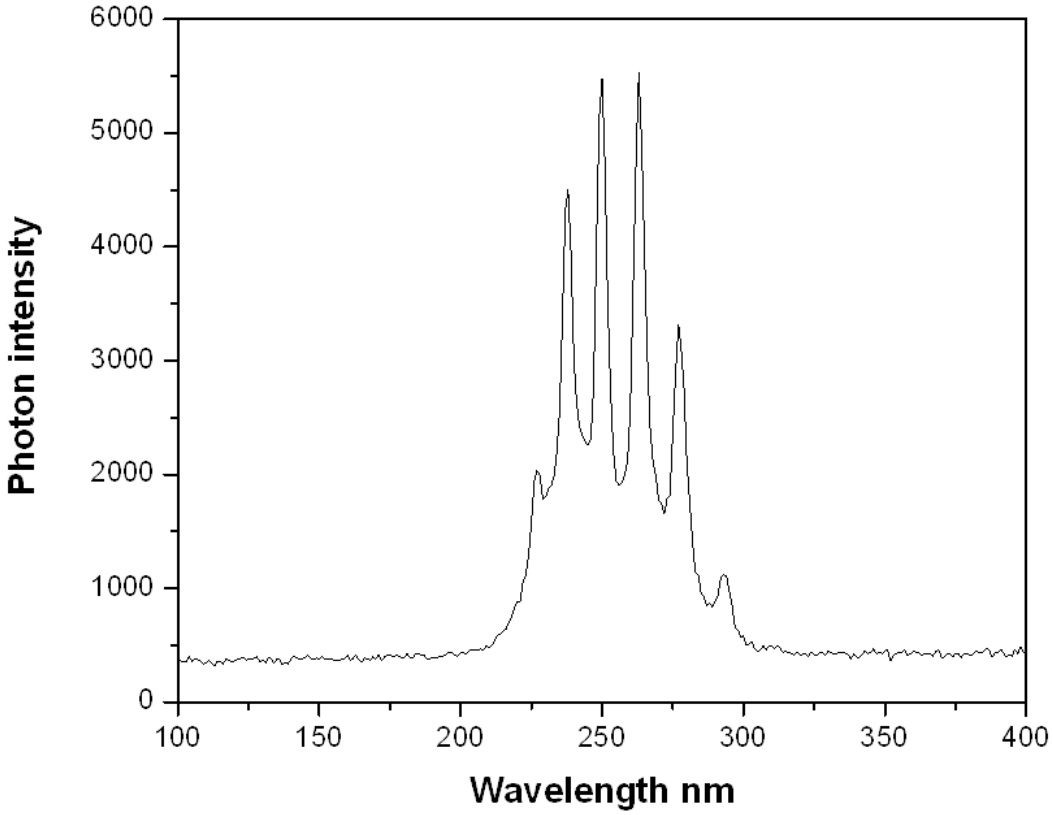

Figures 7A-M. The Raman spectra obtained using the Thermo Scientific DXR SmartRaman spectrometer and the 780 nm laser. A. MoCu CIHT cell anode starting material showing no peak. B. Rinsed anode from the CIHT cell [MoCu (H permeation)/LiOH-LiBr/NiO] that output 14.5 Wh, 100 mA, 150% gain showing a new sharp inverse Raman effect (IRE) absorption peak starting at 1950 cm^{-1} that matches the free rotor energy of $H_2(1/4)$ (0.2414 eV) to four significant figures. C. H_2O sonicated anode from the CIHT cell [MoCu (H permeation)/LiOH-LiBr/NiO] cell that output 14.5 Wh, 100 mA, 150% gain showing the $H_2(1/4)$ 1950 cm^{-1} IRE peak. D. Rinsed anode from the CIHT cell [MoCu (H permeation)/LiOH-LiBr/NiO] cell that output 6.0 Wh, 80 mA, at 190% gain showing the $H_2(1/4)$ 1950 cm^{-1} IRE peak. E. [CoCu (H permeation)/LiOH-LiBr/NiO] that output 6.49 Wh, 150 mA, at 186% gain $H_2(1/4)$ showing the 1950 cm^{-1} IRE peak. F. [MoNiAl (45.5/45.5/9 wt%)/LiOH-LiBr/NiO] that output 2.40 Wh, 80 mA, at 176% gain showing the $H_2(1/4)$ 1950 cm^{-1} IRE peak. G. Certain metal foils and crystalline samples showed a natural abundance $H_2(1/4)$ inverse Raman effect absorption peak having different matrix shifts due to the local environment's influence on the $H_2(1/4)$ inclusion. For example, aluminum foil was discovered to have the IRE peak starting at 1950 cm^{-1} and centered at 1984 cm^{-1}. H. LiOH was discovered to have the IRE peak centered at 2308 cm^{-1}. I. LiOH-LiBr was discovered to have the IRE peak centered at 2608 cm^{-1}. J. Ball milling LiOH-LiBr caused a reaction to greatly intensify the IRE peak and shift it to be centered at 2308 cm^{-1} like LiOH, as well as form a peak centered at 1990 cm^{-1}. K. $Ca(OH)_2$ was discovered to have the IRE peak centered at 2447 cm^{-1}. L. The reaction product from ball milling $Ca(OH)_2 + Li_2CO_3$ was discovered to have the IRE peak centered at 1997 cm^{-1}. M. The products of certain solid fuel reactants such as the product LiHBr showed the $H_2(1/4)$ inverse Raman effect absorption peak centered at 1994 cm^{-1}.

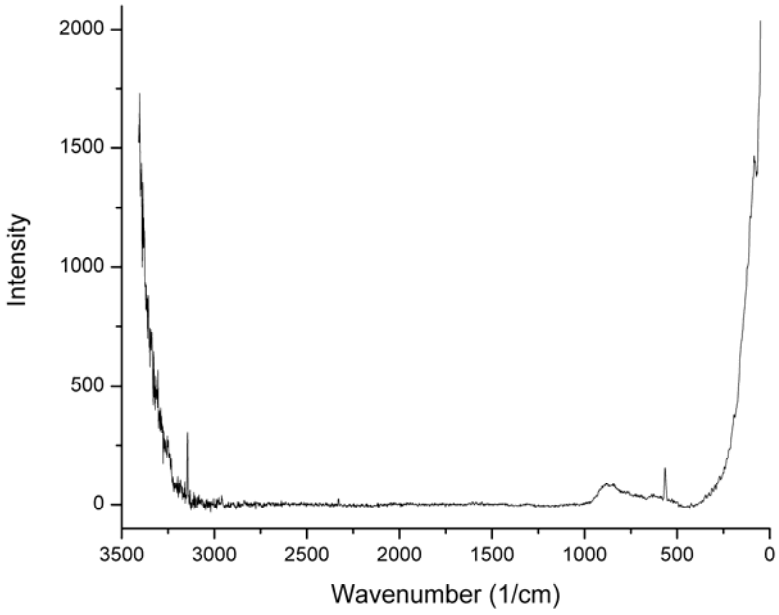
Intensity
2000
1500
1000
500
0
3500
3000
2500
2000
1500
1000
500
0
Wavenumber (1/cm)

A

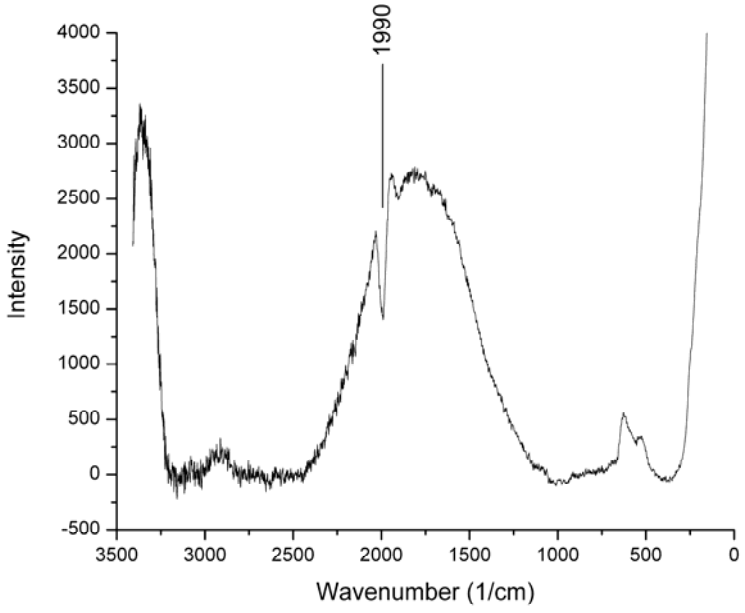
1990
Intensity
4000
3500
3000
2500
2000
1500
1000
500
0
-500
3500
3000
2500
2000
1500
1000
500
0
Wavenumber (1/cm)

B

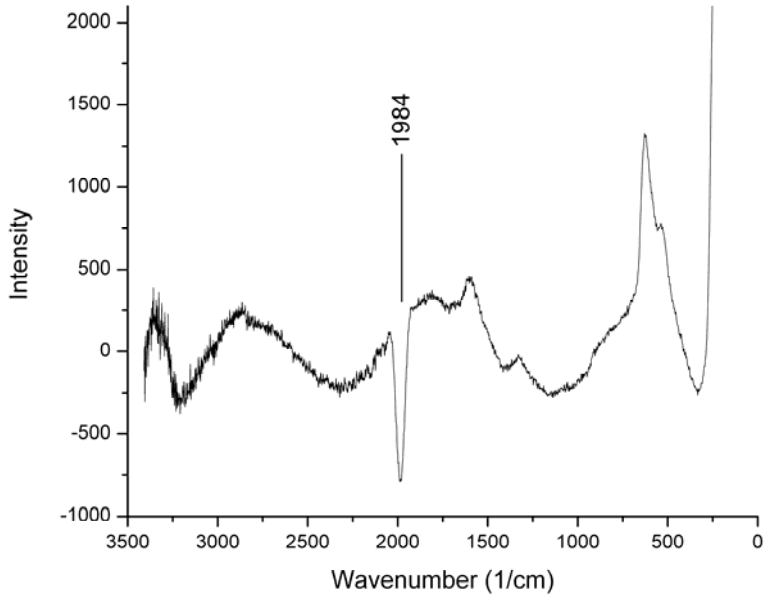
2000
1500
1000
500
0
-500
-1000
Intensity
1984
3500
3000
2500
2000
1500
1000
500
0
Wavenumber (1/cm)

C

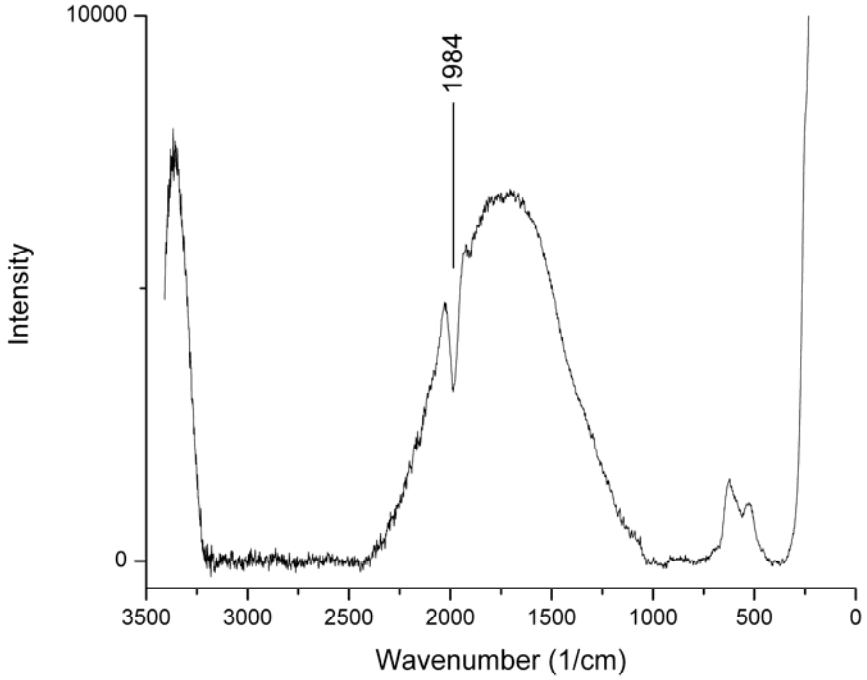
10000
0
Intensity
1984
3500
3000
2500
2000
1500
1000
500
0
Wavenumber (1/cm)

D

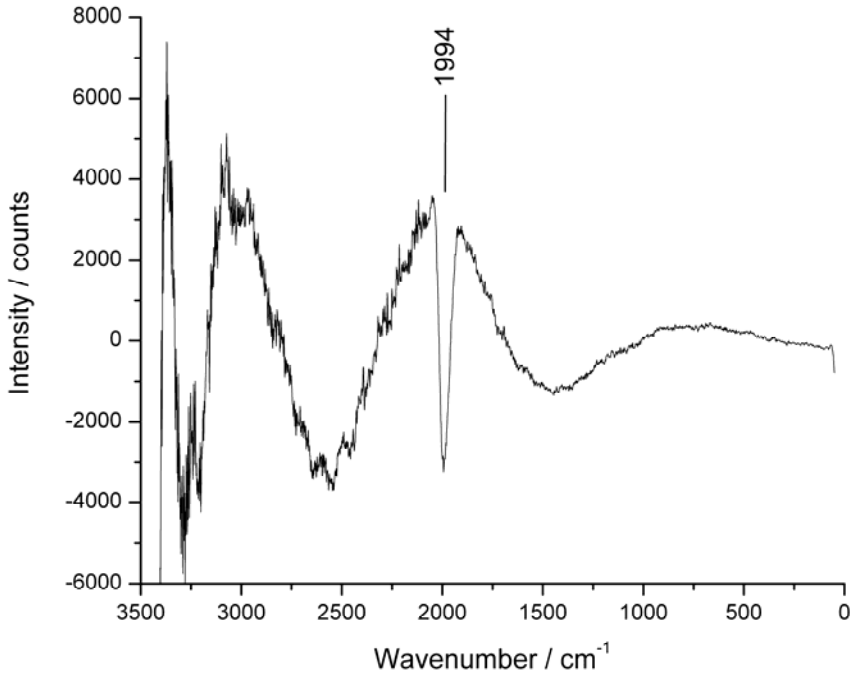
1994
Intensity / counts
Wavenumber / cm-1
8000
6000
4000
2000
0
-2000
-4000
-6000
3500
3000
2500
2000
1500
1000
500
0

E

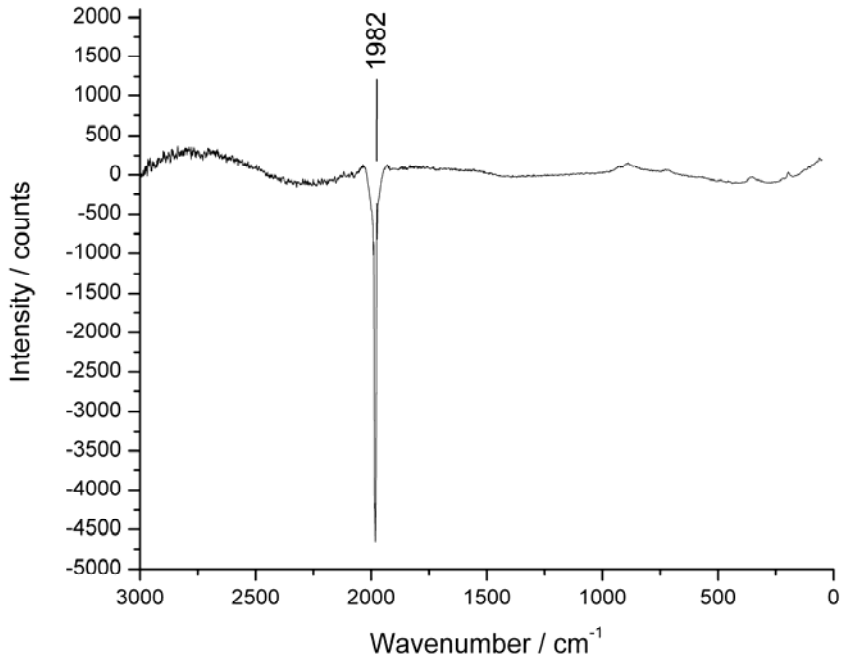
1982
Intensity / counts
Wavenumber / cm-1
2000
1500
1000
500
0
-500
-1000
-1500
-2000
-2500
-3000
-3500
-4000
-4500
-5000
3000
2500
2000
1500
1000
500
0

F

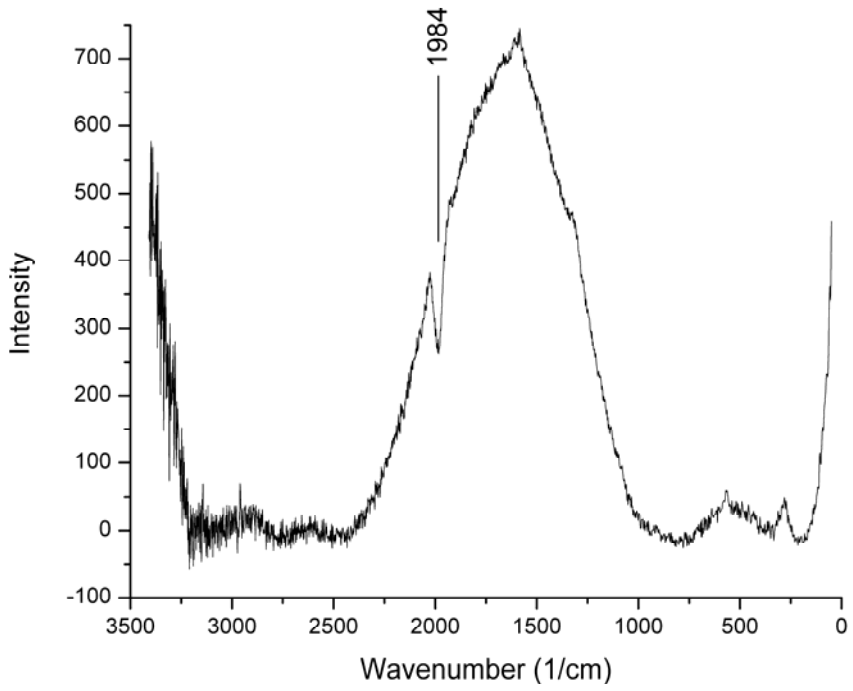
1984
Intensity
Wavenumber (1/cm)
700
600
500
400
300
200
100
0
-100
3500
3000
2500
2000
1500
1000
500
0

G

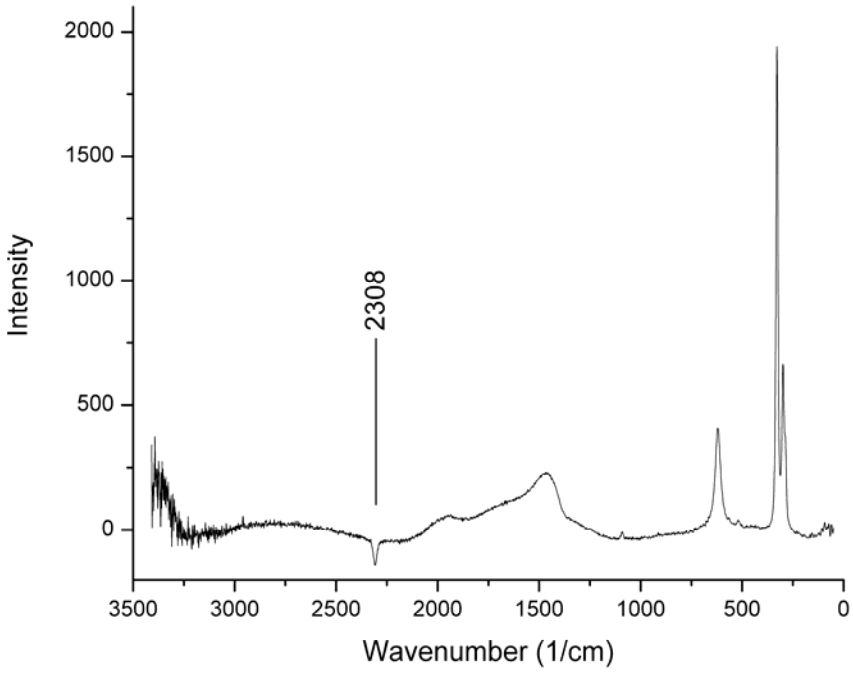
2308
Intensity
Wavenumber (1/cm)
2000
1500
1000
500
0
3500
3000
2500
2000
1500
1000
500
0

H

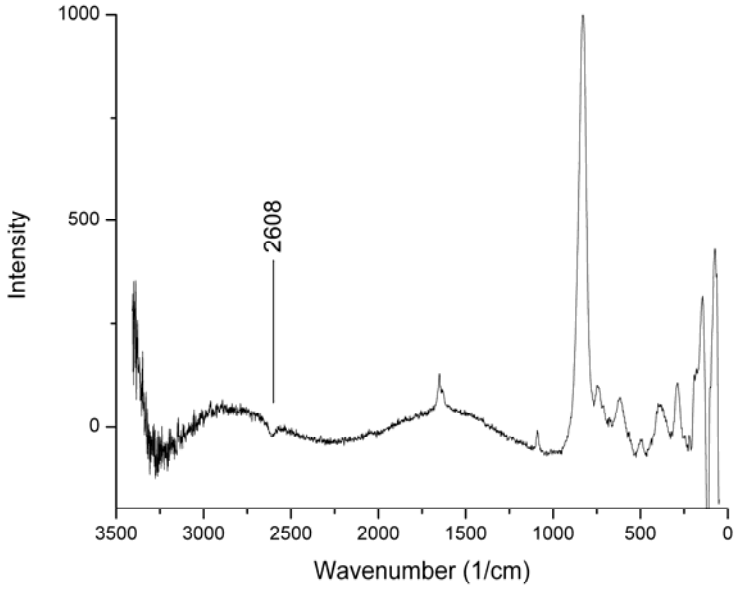
1000
500
0
Intensity
2608
3500
3000
2500
2000
1500
1000
500
0
Wavenumber (1/cm)

I

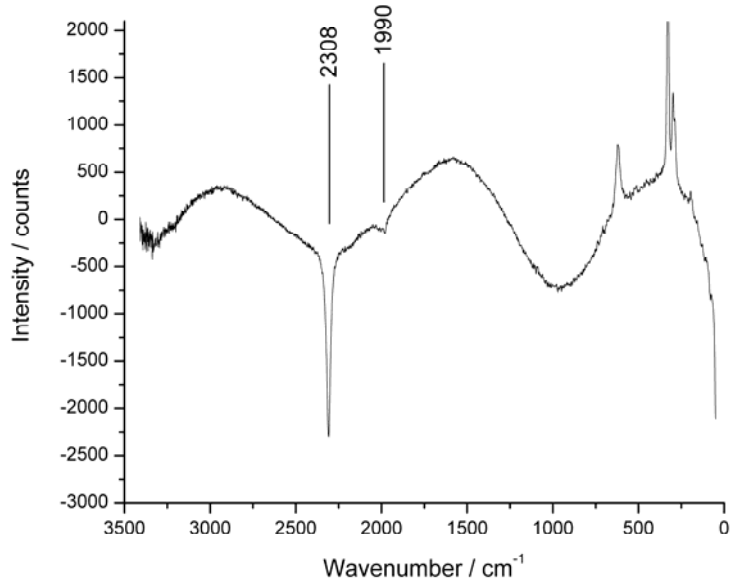
2000
1500
1000
500
0
-500
-1000
-1500
-2000
-2500
-3000
Intensity / counts
2308
1990
3500
3000
2500
2000
1500
1000
500
0
Wavenumber / cm-1

J

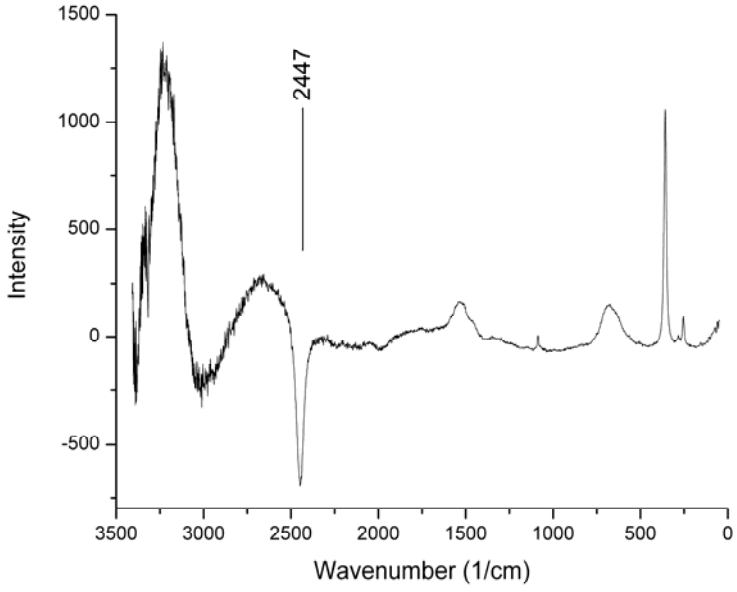
2447
Intensity
Wavenumber (1/cm)

K

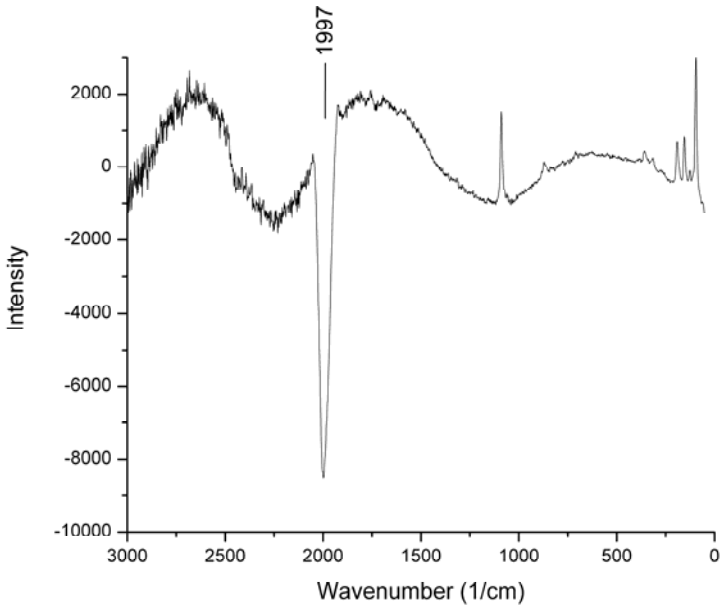
1997
Intensity
Wavenumber (1/cm)

L

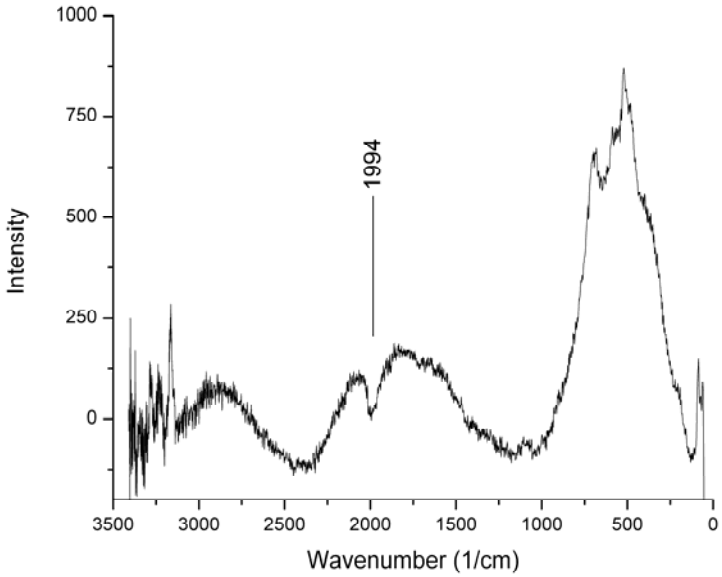
1000
750
500
250
0
Intensity
1994
3500
3000
2500
2000
1500
1000
500
0
Wavenumber (1/cm)

M

Figure 8. ToF-SIMS spectrum of solid fuel Li + $LiNH_2$ + Ru-Al_2O_3 that showed ions arriving before m/e = 1 confirming that the energy release of Eq. (4) is manifest as high kinetic energy H^- of about 204 eV. Other ions such as oxygen (m/e = 16) showed no early peak.

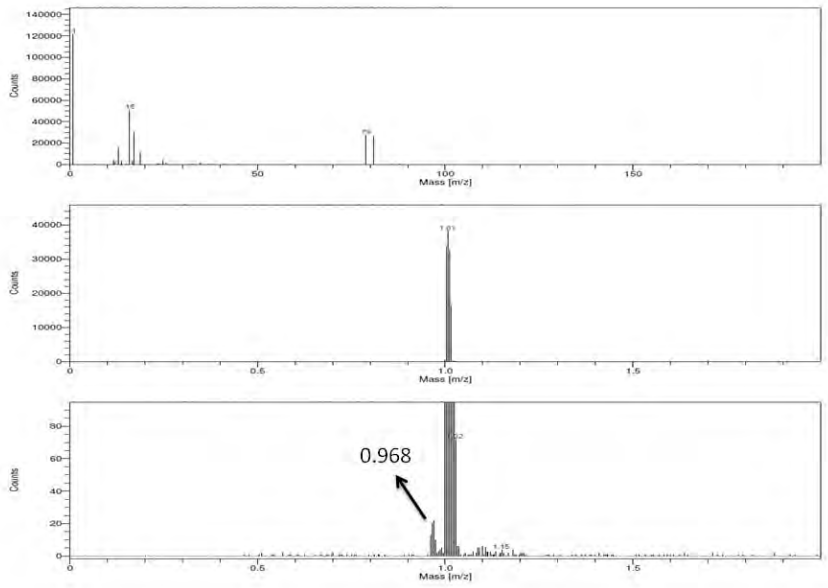

Figures 9A-D. The XPS spectra. A-B. The hydrino solid fuel product LiHBr from two runs showed a peak at 494.5 eV and 495.6 eV assigned to $H_2(1/4)$ wherein other possibilities such Na, Sn, and Zn were eliminated since only Li, Br, O, and C peaks are present and other peaks of the candidates are absent. For example, the Na KLL Auger peak at 493 eV was eliminated due to the complete absence of the typically more intense Na 1s (1072 eV) as well as the Na $2p_{1/2}$ (31 eV) and Na 2s (64 eV). C-D. The CIHT cells [MoCu (H permeation)/LiOH-LiBr/NiO] (1.56 Wh, 50 mA, at 189% gain), and [MoNi (H permeation)/LiOH-LiBr/NiO] (1.53 Wh, 50 mA, at 190%) showed a peak at 496 eV assigned to $H_2(1/4)$ wherein other possibilities such as Mo and Na were eliminated. For example, the 496 eV peak could not be associated with Mo 1s, as its intensity would be much smaller than Mo 3p peaks and the energy would be higher than that observed. The Na KLL Auger peak at 493 eV was eliminated due to the complete absence of the typically more intense Na 1s (1072 eV) as well as the Na $2p_{1/2}$ (31 eV) and Na 2s (64 eV).

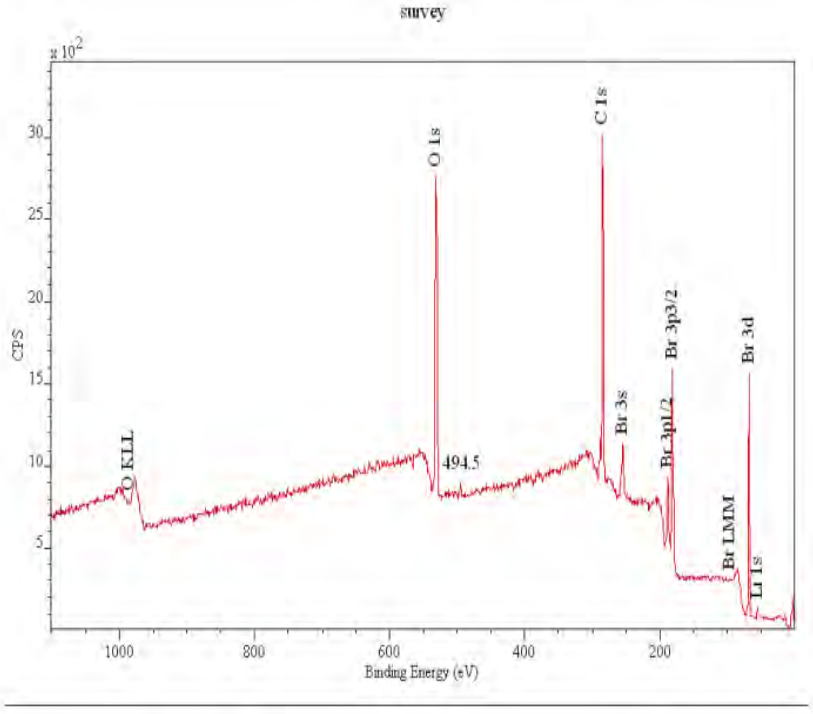

A

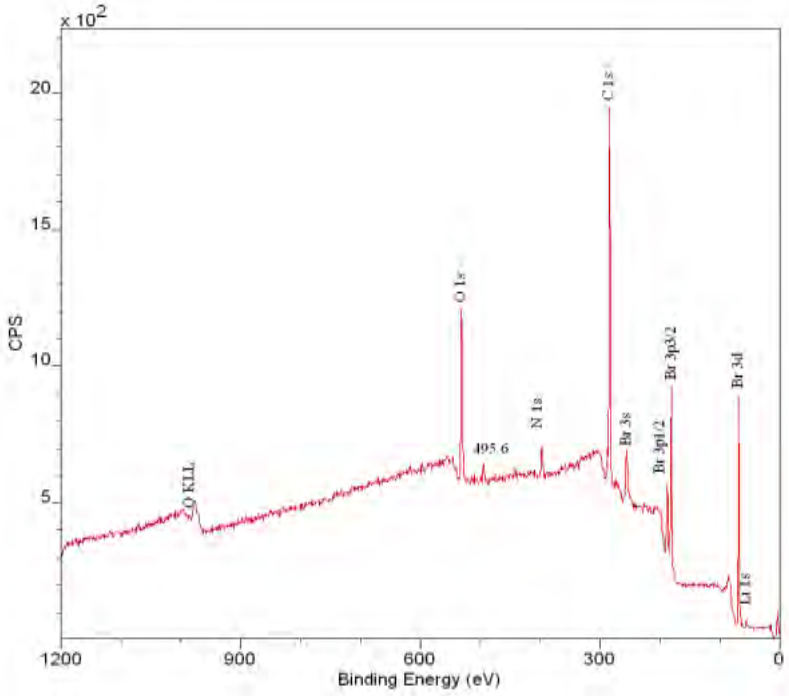
x 10^2
20
15
10
5
CPS
O KLL
O 1s
495.6
N 1s
C 1s
Br 3s
Br 3p1/2
Br 3p3/2
Br 3d
Li 1s
1200
900
600
300
0
Binding Energy (eV)

B

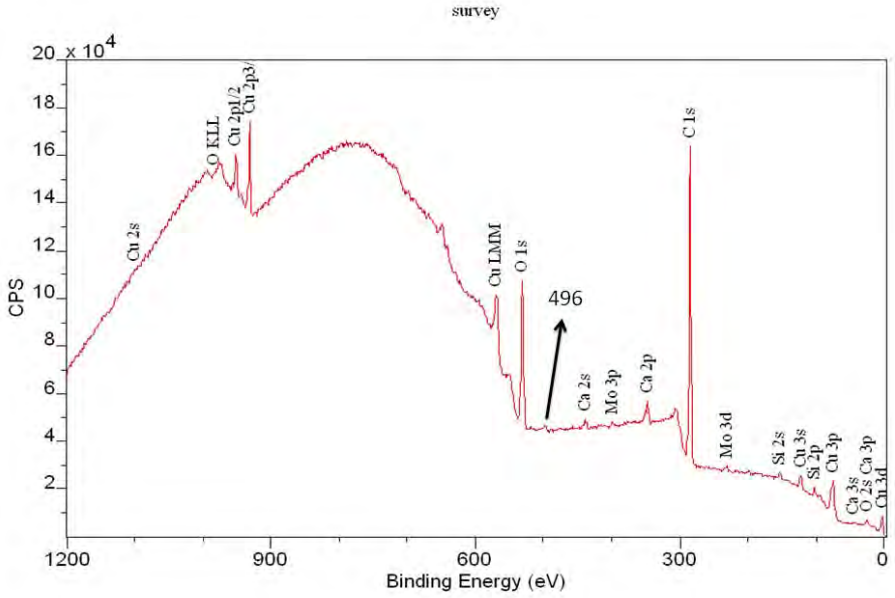
survey
20 x 10^4
18
16
14
12
10
8
6
4
2
CPS
Cu 2s
O KLL
Cu 2p1/2
Cu 2p3/
Cu LMM
O 1s
496
Ca 2s
Mo 3p
Ca 2p
C 1s
Mo 3d
Si 2s
Cu 3s
Si 2p
Cu 3p
Ca 3s
O 2s
Ca 3p
Cu 3d
1200
900
600
300
0
Binding Energy (eV)

C

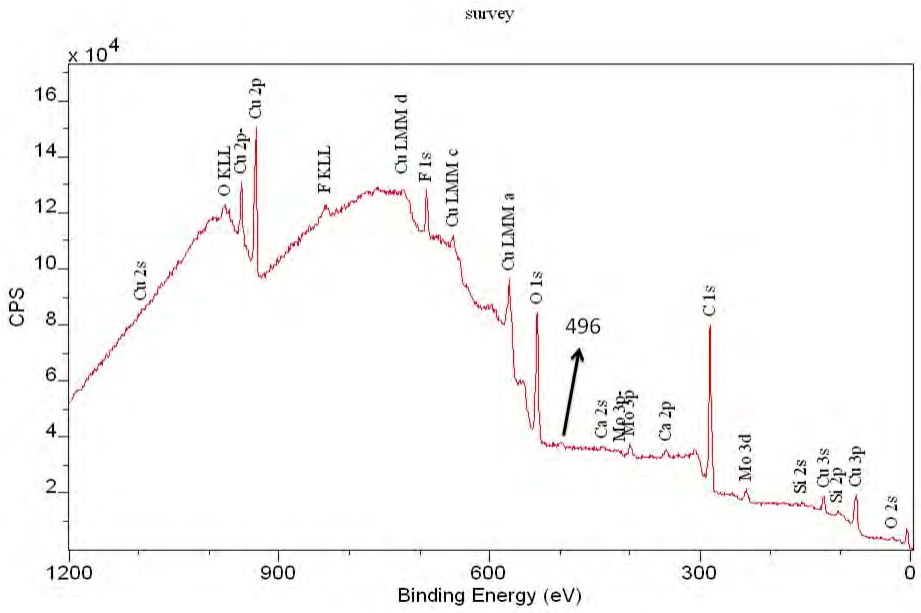
survey
x 10^4
CPS
16
14
12
10
8
6
4
2
1200
900
600
300
0
Binding Energy (eV)
Cu 2s
O KLL
Cu 2p
Cu 2p
F KLL
Cu LMM d
F 1s
Cu LMM c
Cu LMM a
O 1s
496
Ca 2s
Mo 3p
Ca 2p
C 1s
Mo 3d
Si 2s
Cu 3s
Si 2p
Cu 3p
O 2s

D

Figure 10. The FTIR spectrum of solid fuel product LiHBr showing a new sharp peak at 1988 cm^{-1} that is a close match to the free rotor energy of $H_2(1/4)$.

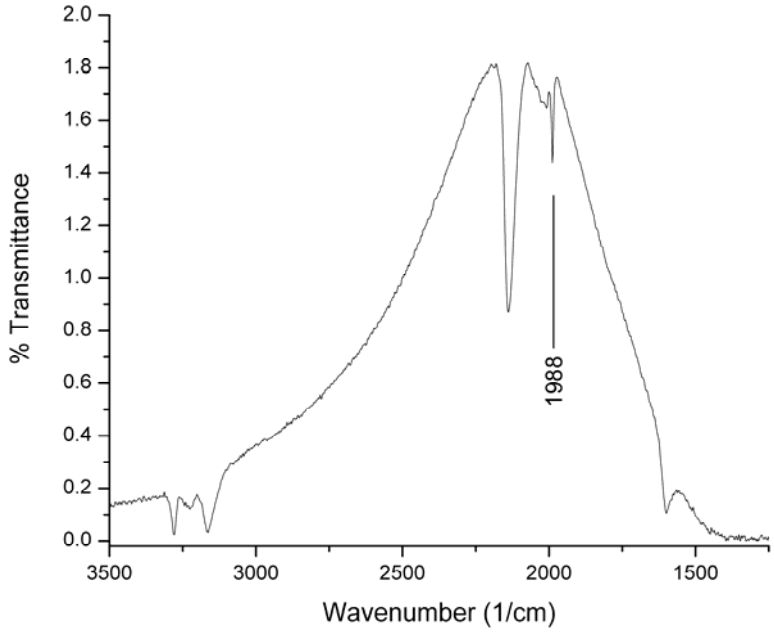

Figures 11A-D. Raman-mode second-order photoluminescence spectra of the KOH-KCl (1:1) getter of CIHT cells. A. [Mo, 10 bipolar plates/LiOH-LiBr-MgO/NiO] that output 2550.5 Wh, 1.7A, 9.5V, at 234% gain. B. [MoCu/LiOH-LiBr-MgO/NiO] that output 3.5 Wh, 80 mA, at 120% gain. C. [MoNi/LiOH-LiBr-MgO/NiO] that output 1.8 Wh, 80 mA, at 140% gain wherein MoNi showed up-field shifted matrix peaks at -4.04 and -4.38 ppm (Figure 5B). D. [CoCu (H permeation)/LiOH-LiBr/NiO] that output 6.49 Wh, 150 mA, at 186% gain that showed up-field shifted matrix peaks at -4.09 and -4.34 ppm (Figure 5C).

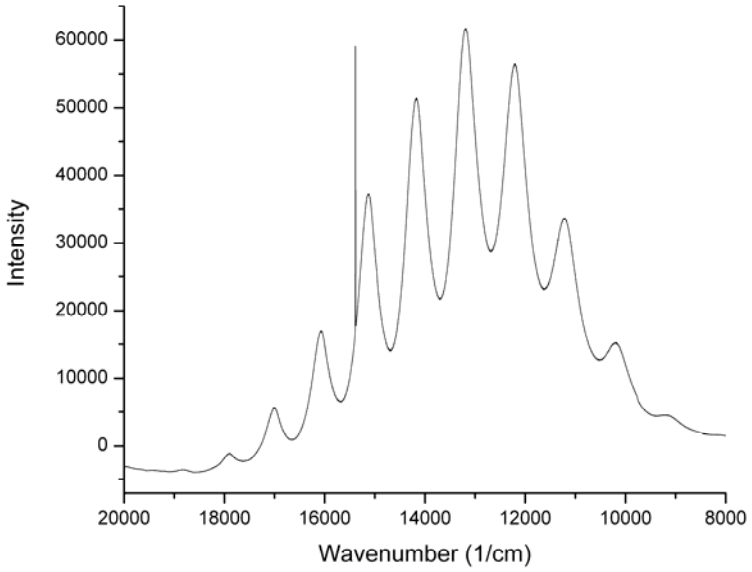

A

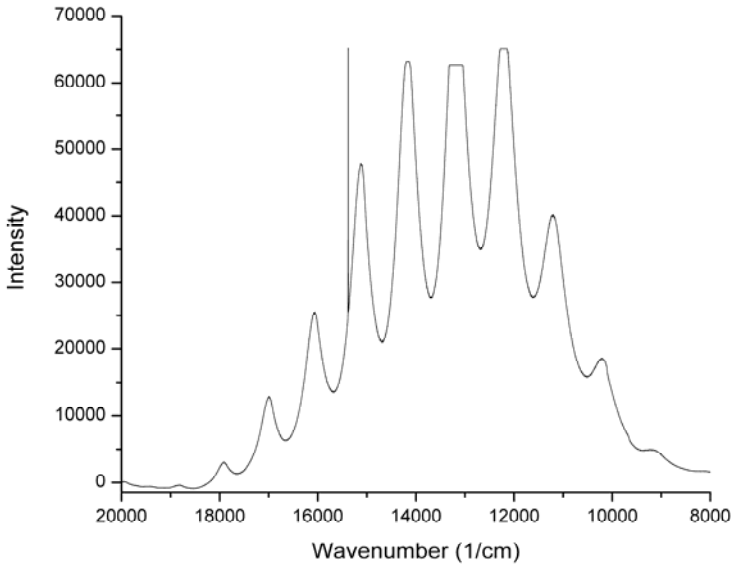

B

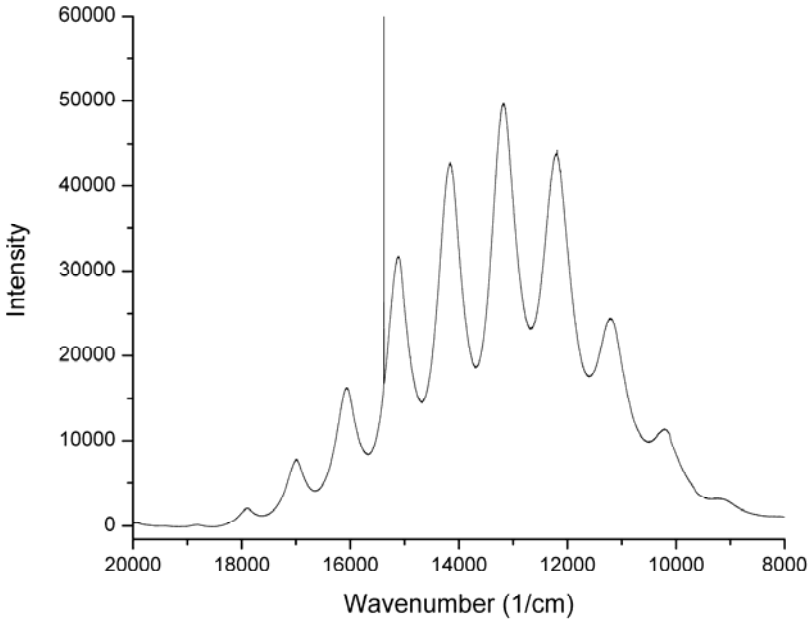
60000
50000
40000
30000
20000
10000
0
Intensity
20000
18000
16000
14000
12000
10000
8000
Wavenumber (1/cm)

C

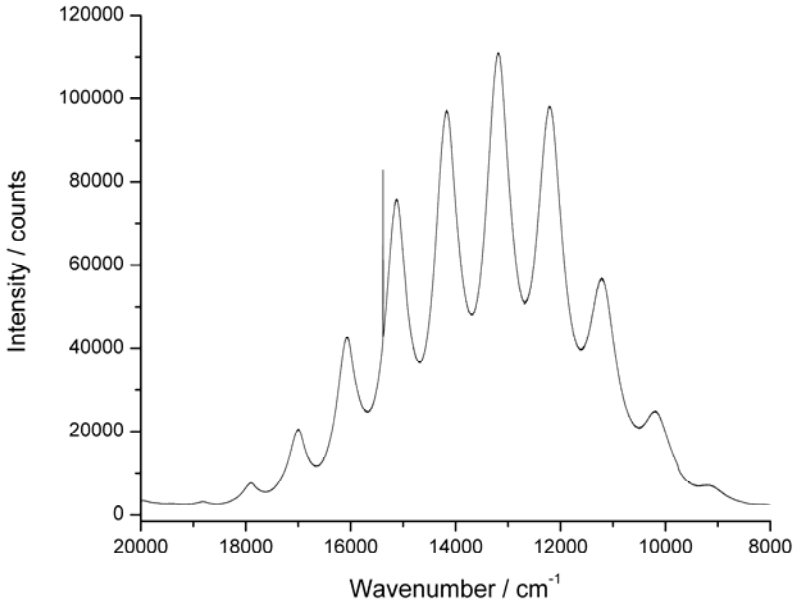
120000
100000
80000
60000
40000
20000
0
Intensity / counts
20000
18000
16000
14000
12000
10000
8000
Wavenumber / cm-1

D